USGS
science for a changing world

# Field-Trip Guide for Exploring Pyroclastic Density Current Deposits from the May 18, 1980, Eruption of Mount St. Helens, Washington

Scientific Investigations Report 2017–5022–C

U.S. Department of the Interior
U.S. Geological Survey

**Cover.** View of Mount St. Helens crater, with May 18, 1980, pyroclastic density current deposits exposed along the drainage. The photo was taken at UTM 560985.19 E., 5122505.17 N., looking south.

# Field-Trip Guide for Exploring Pyroclastic Density Current Deposits from the May 18, 1980, Eruption of Mount St. Helens, Washington

By Brittany D. Brand, Nicholas Pollock, Damiano Sarocchi, Josef Dufek, and Michael A. Clynne

Scientific Investigations Report 2017–5022–C

**U.S. Department of the Interior**
**U.S. Geological Survey**

**U.S. Department of the Interior**
RYAN K. ZINKE, Secretary

**U.S. Geological Survey**
William H. Werkheiser, Acting Director

U.S. Geological Survey, Reston, Virginia: 2017



Suggested citation:
Brand, B.D., Pollock, Nicholas, Sarocchi, Damiano, Dufek, Josef, and Clynne, M.A., 2017, Field-Trip guide for exploring pyroclastic density current deposits from the May 18, 1980, eruption of Mount St. Helens, Washington: U.S. Geological Survey Scientific Investigations Report 2017–5022–C, 34 p., https://doi.org/10.3133/sir20175022C.

ISSN 2328 0328 (online)

# Preface

The North American Cordillera is home to a greater diversity of volcanic provinces than any comparably sized region in the world. The interplay between changing plate-margin interactions, tectonic complexity, intra-crustal magma differentiation, and mantle melting have resulted in a wealth of volcanic landscapes. Field trips in this series visit many of these landscapes, including (1) active subduction-related arc volcanoes in the Cascade Range; (2) flood basalts of the Columbia Plateau; (3) bimodal volcanism of the Snake River Plain-Yellowstone volcanic system; (4) some of the world's largest known ignimbrites from southern Utah, central Colorado, and northern Nevada; (5) extension-related volcanism in the Rio Grande Rift and Basin and Range Province; and (6) the spectacular eastern Sierra Nevada featuring Long Valley Caldera and the iconic Bishop Tuff. Some of the field trips focus on volcanic eruptive and emplacement processes, calling attention to the fact that the western United States provides opportunities to examine a wide range of volcanological phenomena at many scales.

The 2017 Scientific Assembly of the International Association of Volcanology and Chemistry of the Earth's Interior (IAVCEI) in Portland, Oregon, marks the first time that the U.S. volcanological community has hosted this quadrennial meeting since 1989, when it was held in Santa Fe, New Mexico. The 1989 field-trip guides are still widely used by students and professionals alike. This new set of field guides is similarly a legacy collection that summarizes decades of advances in our understanding of magmatic and tectonic processes of volcanic western North America.

The field of volcanology has flourished since the 1989 IAVCEI meeting, and it has profited from detailed field investigations coupled with emerging new analytical methods. Mapping has been enhanced by plentiful major- and trace-element whole-rock and mineral data, technical advances in radiometric dating and collection of isotopic data, GPS (Global Positioning System) advances, and the availability of lidar (light detection and ranging) imagery. Spectacularly effective microbeam instruments, geodetic and geophysical data collection and processing, paleomagnetic determinations, and modeling capabilities have combined with mapping to provide new information and insights over the past 30 years. The collective works of the international community have made it possible to prepare wholly new guides to areas across the western United States. These comprehensive field guides are available, in large part, because of enormous contributions from many experienced geologists who have devoted entire careers to their field areas. Early career scientists are carrying forward and refining their foundational work with impressive results.

Our hope is that future generations of scientists as well as the general public will use these field guides as introductions to these fascinating areas and will be enticed toward further exploration and field-based research.

Michael Dungan, University of Oregon
Judy Fierstein, U.S. Geological Survey
Cynthia Gardner, U.S. Geological Survey
Dennis Geist, National Science Foundation
Anita Grunder, Oregon State University
John Wolff, Washington State University

Field-trip committee, IAVCEI 2017

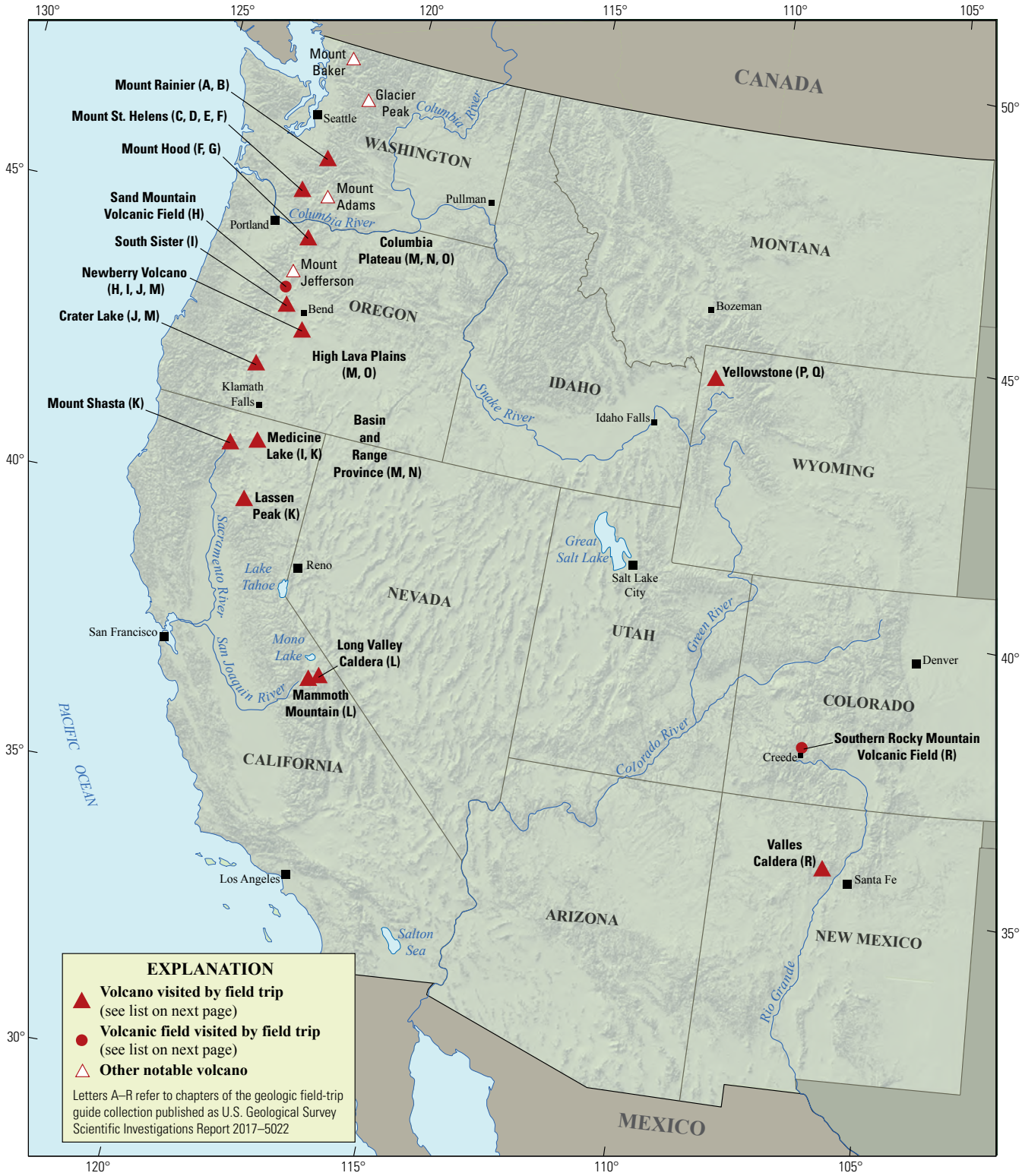


Map of the western United States showing volcanoes and volcanic fields visited by geologic field trips scheduled in conjunction with the 2017 meeting of the International Association of Volcanology and Chemistry of the Earth's Interior (IAVCEI) in Portland, Oregon, and available as chapters in U.S. Geological Survey Scientific Investigations Report 2017–5022.

# Contributing Authors

**Boise State University**
Brittany D. Brand
Nicholas Pollock

**Colgate University**
Karen Harpp
Alison Koleszar

**Durham University**
Richard J. Brown

**East Oregon University**
Mark L. Ferns

**ETH Zurich**
Olivier Bachmann

**Georgia Institute of Technology**
Josef Dufek

**GNS Science, New Zealand**
Natalia I. Deligne

**Hamilton College**
Richard M. Conrey

**Massachusetts Institute of Technology**
Timothy Grove

**National Science Foundation**
Dennis Geist (also with Colgate University and University of Idaho)

**New Mexico Bureau of Geology and Mineral Resources**
Paul W. Bauer
William C. McIntosh
Matthew J. Zimmerer

**New Mexico State University**
Emily R. Johnson

**Northeastern University**
Martin E. Ross

**Oregon Department of Geology and Mineral Industries**
William J. Burns
Lina Ma
Ian P. Madin
Jason D. McClaughry

**Oregon State University**
Adam J.R. Kent

**Portland State University**
Jonathan H. Fink
Martin J. Streck
Ashley R. Streig

**San Diego State University**
Victor E. Camp

**Smithsonian Institution**
Lee Siebert

**Universidad Nacional Autónoma de San Luis Potosi**
Damiano Sarocchi

**University of California, Davis**
Kari M. Cooper

**University of Liverpool**
Peter B. Kokelaar

**University of Northern Colorado**
Steven W. Anderson

**University of Oregon**
Ilya N. Binderman
Michael A. Dungan
Daniele McKay (also with Oregon State University and Oregon State University, Cascades)

**University of Portland**
Kristin Sweeney

**University of Tasmania**
Martin Jutzeler
Jocelyn McPhie

**University of Utah**
Jamie Farrell

**U.S. Army Corps of Engineers**
Keith I. Kelson

**U.S. Forest Service**
Gordon E. Grant (also with Oregon State University
Robert A. Jensen

**U.S. Geological Survey**
Charles R. Bacon
Andrew T. Calvert
Christine F. Chan
Robert L. Christiansen
Michael A. Clynne
Michael A. Cosca
Julie M. Donnelly-Nolan
Benjamin J. Drenth
William C. Evans
Judy Fierstein
Cynthia A. Gardner
V.J.S. Grauch
Christopher J. Harpel
Wes Hildreth
Richard P. Hoblitt
Peter W. Lipman
Jacob B. Lowenstern
Jon J. Major
Seth C. Moran
Lisa A. Morgan
Leah E. Morgan
L.J. Patrick Muffler
James E. O'Connor
John S. Pallister
Thomas C. Pierson
Joel E. Robinson
Juliet Ryan-Davis
Kevin M. Scott
William E. Scott
Wayne (Pat) Shanks
David R. Sherrod
Thomas W. Sisson
Mark Evan Stelten
Weston Thelen
Ren A. Thompson
Kenzie J. Turner
James W. Vallance
Alexa R. Van Eaton
Jorge A. Vazquez
Richard B. Waitt
Heather M. Wright

**U.S. Nuclear Regulatory Commission**
Stephen Self (also with University of California, Berkeley)

**Washington State University**
Joseph R. Boro
Owen K. Neill
Stephen P. Reidel
John A. Wolff

**Acknowledgments**
Juliet Ryan-Davis and Kate Sullivan created the overview map, and Vivian Nguyen created the cover design for this collection of field-trip guide books. The field trip committee is grateful for their contributions.

# Contents

## Figures

## Tables



# Conversion Factors

| Multiply | By | To obtain |
|---|---|---|
| | Length | |
| centimeter (cm) | 0.3937 | inch (in.) |
| millimeter (mm) | 0.03937 | inch (in.) |
| meter (m) | 3.281 | foot (ft) |
| kilometer (km) | 0.6214 | mile (mi) |
| meter (m) | 1.094 | yard (yd) |
| | Area | |
| square kilometer ($km^2$) | 0.3861 | square mile ($mi^2$) |
| | Volume | |
| cubic kilometer ($km^3$) | 0.2399 | cubic mile ($mi^3$) |

# Abbreviations

| | |
|---|---|
| LROG | Laser Remote Optical Granulometry |
| PDB | proximal bedded deposits |
| PDC | pyroclastic density current |
| USGS | U.S. Geological Survey |

# Field-Trip Guide for Exploring Pyroclastic Density Current Deposits from the May 18, 1980, Eruption of Mount St. Helens, Washington

By Brittany D. Brand[1], Nicholas Pollock[1], Damiano Sarocchi[2], Josef Dufek[3], and Michael A. Clynne[4]

## Abstract

Pyroclastic density currents (PDCs) are one of the most dangerous phenomena associated with explosive volcanism. To help constrain damage potential, a combination of field studies, laboratory experiments, and numerical modeling are used to establish conditions that influence PDC dynamics and depositional processes, including runout distance. The objective of this field trip is to explore field relations that may constrain PDCs at the time of emplacement.

The PDC deposits from the May 18, 1980, eruption of Mount St. Helens are well exposed along the steep flanks (10–30° slopes) and across the pumice plain (5–12° slopes) as far as 8 km north of the volcano. The pumice plain deposits represent deposition from a series of concentrated PDCs and are primarily thick (3–12 m), massive, and poorly sorted. In contrast, the steep east-flank deposits are stratified to cross-stratified, suggesting deposition from PDCs where turbulence strongly influenced transport and depositional processes.

The PDCs that descended the west flank were largely nondepositional; they maintained a higher flow energy and carrying capacity than PDCs funneled through the main breach, as evidenced by the higher concentration of large blocks in their deposits. The PDC from the west flank collided with PDCs funneled through the breach at various points along the pumice plain. Evidence for flow collision will be explored and debated throughout the field trip.

Evidence for substrate erosion and entrainment is found (1) along the steep eastern flank of the volcano, which has a higher degree of rough, irregular topography relative to the west flanks where PDCs were likely nonerosive, (2) where PDCs encountered debris-avalanche hummocks across the pumice plain, and (3) where PDCs eroded and entrained material deposited by PDCs produced during earlier phases of the eruption. Two features interpreted as large-scale (tens of meters wide) levees and a large (~200 m wide) channel scour-and-fill feature provide the first evidence of self-channelization within PDCs sustained for minutes to tens of minutes (total volume of deposits is ~0.12 km$^3$; area covered is ~15.5 km$^2$; Rowley and others, 1981).

Our ability to interpret the deposits of PDCs is critical for understanding transport and depositional processes that control PDC dynamics. The results of extensive work on the May 18, 1980, PDC deposits show that slope and irregular topography strongly influence PDC flow path, dynamics, criticality (for example, supercritical versus subcritical), carrying capacity, and erosive capacity. However, the influence of these conditions on ultimate flow runout and damage potential warrants further exploration through the combination of field, experimental, and numerical approaches.

## Introduction

Our ability to interpret the deposits of pyroclastic density currents (PDCs) is critical for understanding the transport, erosional, and depositional processes that control PDC dynamics. We will use the May 18, 1980, pyroclastic density current (PDC) deposit characteristics to interpret and discuss the transport and depositional mechanisms within the depositional (basal) region of the currents that produced them. The excellent exposures at Mount St. Helens also allow us to explore the influence of surface roughness, substrate erosion, and self-channelization as they are recorded in the PDC deposits and to assess the influence of these factors on current mobility and runout distance. The objective of this field trip is to explore field relations that can be used to constrain PDC conditions at the time of emplacement. Field discussions will result in new ideas and hypotheses to test using experiments and numerical modeling.

## Physical-Intensity-Level Disclaimer

Access to the sites in this field guide requires excellent physical fitness and the ability to hike long distances (12 to 20 km roundtrip each day for three days). The terrain is rough (boulder-strewn drainages and steep talus slopes) and there is often no shade. The steepest part of our hikes climbs ~350 m over a distance of 1.75 km to enter the eastern part of the crater.

[1]Department of Geosciences, Boise State University.

[2]Instituto de Geología, Universidad Autónoma de San Luis Potosi (Mexico).

[3]Earth and Atmospheric Sciences, Georgia Institute of Technology.

[4]U.S. Geological Survey.

# Brief Eruptive History of Mount St. Helens

Mount St. Helens has been the most active volcano in the Cascade Range during the last 4,000 years. D.R. Mullineaux and D.R. Crandell established the general eruptive history of Mount St. Helens in the 1960s–1980s through their extensive studies of the tephra deposits found around the volcano. They recognized that the eruptive history was episodic, grouped the tephras into "sets" of similar age and composition (Mullineuax, 1996, and references therein) that they described as a series of eruptive stages and periods, and correlated some of the lava flows, domes, and fragmental deposits (Crandell, 1987). Radiocarbon dating provided some geochronologic control, but Crandell and Mullineaux's work was hindered by the lack of preserved tephras older than ~60 ka, because these had been removed by glaciation. Thus the findings of Mullineaux and Crandell suggested that Mount St. Helens was about 40,000–50,000 years old.

New geologic mapping, aided by argon geochronology, paleomagnetic directional data, and additional radiocarbon chronology, established that Mount St. Helens had a much longer eruptive history than recognized by Crandell and Mullineaux (Clynne and others, 2008, and references therein). A variety of deposits and rocks as old as 272,000 years were discovered beneath younger deposits and in lahars. Table 1 presents the results of both Crandell and Mullineaux's seminal work and the refinements added by new mapping and chronology. All dates provided below are summarized in Clynne and others (2005).

The Mount St. Helens lavas are particularly difficult to date by the Ar-Ar method (Layer and Gardner, 2001). In addition to being young, they generally have low $K_2O$ and often contain excess argon in inherited crystals (Clynne and others, 2008). In general, more dating has tended to extend the stages and close the gaps (dormant intervals) between them, and additional chronology is likely to continue to refine these intervals. The eruptive history reported by Crandell and Mullineaux emphasized the major Plinian eruptions of the volcano for which it is famous, but each of those eruptions was followed by a significant period of less explosive and effusive activity. Brief descriptions of each stage and period follow. Note that capital letters refer to sets (for example, Set Y); whereas, lowercase letters refer to layers within a set (for example, Yn).

## Ape Canyon Stage

During the Ape Canyon stage, Mount St. Helens produced a variety of quartz-bearing biotite and (or) hornblende dacites and Set C tephras. These are found as glaciated remnants beneath younger rocks on the southwest flank of Mount St. Helens. The oldest and most prominent of these is Goat Mountain (272±1 ka). Most dated Ape Canyon rocks are found as clasts in lahars in the Lewis River valley or in glacial deposits. Ape Canyon stage rocks found as lithic clasts in younger Plinian deposits and an 84.2±21.9-ka dacite exposed in the crater floor indicate that Ape Canyon stage rocks underlie the present edifice. Zircon, as old as ~500 ka in some of the Ape Canyon rocks, suggests that volcanism or intrusion at Mount St. Helens began well before 272 ka (Claiborne and others, 2010).

## Cougar Stage

During the Cougar stage, Mount St. Helens produced a variety of hypersthene-hornblende dacite domes, pumiceous pyroclastic flows, Sets K and M tephras, and at least two andesite lava flows. A large debris avalanche dated at ~24.5 ka on the southwest flank of the volcano blocked the Lewis River. The debris avalanche was immediately followed by emplacement of several cubic kilometers of pumiceous pyroclastic flows. Breaching of the blockage released large breakout lahars down the Lewis River. The 0.75 $km^3$ Swift Creek andesite lava flow on the south flank was the largest in Mount St. Helens history. Olivine-bearing inclusions in a Cougar stage andesite lava flow found in Pine Creek mark the first unambiguous appearance of a mafic component in the Mount St. Helens magmatic system.

## Swift Creek Stage

During the Swift Creek stage, the widespread Sets S and J tephra were erupted, and three extensive fans of fragmental debris were emplaced on the flanks of Mount St. Helens from hypersthene-hornblende dacite domes. The Crescent Ridge fan on the west to northwest flank was derived from the Crescent Dome, which is preserved on the west flank. Swift Creek stage domes exposed in the east crater wall may have been the source of the Cedar Flats fan on the northeast to southeast flank of the volcano and in the Lewis River valley. The source of the Swift Creek fan on the south flank is unknown. Most fan material originated as block-and-ash flows, but much material in the distal parts of the fans was remobilized as lahars. Details of the Swift Creek stage are still not well known, but subtle differences in the lithologies suggest that the three fans represent three discrete periods of eruption between about 16 and 10 ka.

## Spirit Lake Stage

The Spirit Lake stage is the youngest stage of Mount St. Helens and is the most studied interval of the eruptive history, because it is well exposed and dated. The Spirit Lake stage is divided into seven eruptive periods separated by short noneruptive intervals (table 1): (1) Smith Creek period, ~3,900–3,300 yr B.P.; (2) Pine Creek period, ~3,000–2,550 yr B.P.; (3) Castle Creek period, 2,025–1,700 yr B.P.; (4) Sugar Bowl period, ~1,050 yr B.P. (eruptive age range unconstrained, although paleomagnetic studies suggest a short eruptive period); (5) Kalama period, 1479–~1725 C.E.; (6) Goat Rocks period, 1800–1857 C.E.; and (7) modern period, 1980–2008 C.E.

During the Smith Creek period, Mount St. Helens erupted a series of dacite tephras, Set Y, which included the largest

**Table 1.** Mount St. Helens, Washington, eruptive history (modified from Clynne and others, 2008). Includes only the major eruptive products of each period. Some of the geochronology is still not accepted, especially during the Swift Creek Period. As more geochronology has been obtained the dormant intervals have shrunk, and it is likely that there was minor eruptive activity during dormant intervals.

| Eruptive stage | Eruptive period | Ash set | Major eruptive products |
|---|---|---|---|
| Spirit Lake 3,900–0 yr B.P. | Modern period 1980–2008 C.E. | 1980 | Lateral blast and debris avalanche, pyroclastic flows, dacite domes, lahars |
| | Goat Rocks period 1800–1857 C.E. | Layer T | Andesite flows, dacite dome and block and ash flows |
| | Kalama period 1479–1725 C.E. | Sets W and X, layer z | Dacite domes, pyroclastic flows, and block and ash flows, andesite flows, lahars |
| | Sugar Bowl period 1,050–1,000 yr B.P. | Layer D | Dacite domes, lateral blast |
| | Castle Creek period 2,025–1,700 yr B.P. | Set B | Dacite domes and flows, block and ash flows, basalt to andesite flows, lahars |
| | Pine Creek period 3,000–2,550 yr B.P. | Set P and Set B | Dacite domes and block and ash flows, andesite flows, debris avalanches, lahars |
| | Smith Creek period 3,900–3,300 yr B.P. | Set Y | Dacite domes and block and ash flows, pyroclastic flows, lahars |
| | Dormant interval 10–3.9 ka | | |
| Swift Creek 16–10 ka | | Sets S and J | Dacite domes and block and ash flows, pyroclastic flows, lahars |
| | Dormant interval 18–16 ka | | |
| Cougar 28–18 ka | | Sets K and M | Dacite domes and block and ash flows, debris avalanche and pyroclastic flows, andesite flows, lahars |
| | Dormant interval 35–28 ka | | |
| Ape Canyon 300–35 ka | Possible dormant interval 240–160 ka | Set C | Dacite domes and block and ash flows, lahars |

single eruption in its history, Yn ~4 km$^3$. The Smith Creek period began around 3,900 yr B.P. with eruption of several early Set Y tephras. Yn erupted ~3,500 yr B.P., and Ye, another large Plinian event, erupted at ~3,350 yr B.P. Pyroclastic flows, lava domes, and lahars were emplaced after each of the major Set Y events. A fan of fragmental material on the north flank formed ancestral Spirit Lake.

During the early Pine Creek period, Mount St. Helens erupted an extensive series of dacite domes and tephra Set P, followed by a later series of andesitic lava flows, pyroclastic flows, lahars, and tephras Bh and Bo. Pine Creek age dacite domes are exposed in the 1980 crater walls and extensive fans of lithic pyroclastic material and associated lahars are present in Pine Creek and Castle Creek drainages. Two small debris avalanches resulted from collapses of Pine Creek age domes. Damming of Spirit Lake by one of these fans or avalanches resulted in huge lake-breakout lahars in the lower Toutle River valley. The dacitic phase of the Pine Creek activity took place over most of the interval between ~3,000 yr B.P. and 2,550 yr B.P. At about 2,550 yr B.P., the dacitic activity was followed by tephra Bh, abundant andesite lava flows and tephra Bo, and more basaltic andesite to andesite lava flows and lahars. Much of the andesitic fragmental material seen in the 1980 crater walls was erupted during a short interval beginning around 2,550 yr B.P.

The Castle Creek period was the most complex and compositionally diverse period of the Spirit Lake stage. Compositions from dacite to basalt erupted over an ~325-year-long period between ~2025 and ~1,700 yr B.P. in three phases: early, middle, and late. The early phase was primarily dacitic and includes the Northwest Dome and Dogs Head dacite domes and pumiceous and lithic pyroclastic flows, several andesite/dacite lava flows (Redrock Pass and North Rim), and tephra Bi, all probably deposited in the interval ~2,025–1,990 yr B.P. Deposits of the middle Castle Creek period are confined to the south flank of the volcano. This phase was initiated by eruption of basaltic tephra Bu 1 and followed by three units of mafic lava flows: basalts and basaltic andesites of the south flank, pre-Cave Basalt and basaltic andesite, and Cave Basalt. These eruptions took place shortly before and at ~1,895 yr B.P.

During the late Castle Creek period, Mount St. Helens erupted eight (possibly nine) units of basalt to andesite on the north and east flanks of the volcano. In order of eruption, these are (1) andesite of section 26, (2) basaltic andesite of Truman Trail, (3) tephra Bu 2 and basalt of the north flank, (4) andesite of the Plains of Abraham, (5) andesite of Sasquatch

Steps, (6) tephra Bu 3 and basalt of Castle Creek, (7) basaltic andesite of Nelson Glacier, and (8) andesite of Loowit Creek. The Baguette flow, a pyroxene andesite of uncertain age on the southwest flank, is compositionally similar to andesite of Sasquatch Steps and may be related to the late Castle Creek period. These eruptions took place between ~1,895 yr B.P. and ~1700 C.E. Four radiocarbon ages for units (5) and (6) above range from 1,795±30 to 1,730±35 yr B.P., and paleomagnetic directional data suggest that this period of volcanism was short. Late Castle Creek period lava flows cap parts of the modern crater rim. During the Sugar Bowl period, at least three dacite lava domes erupted: Sugar Bowl dome, East Dome, and West Dome. A small lateral blast and tephra layer D were associated with emplacement of Sugar Bowl Dome. The Sugar Bowl period was probably short lived and occurred from ~1,050 to ~1,000 yr BP.

The Kalama period is described as three phases of activity—early, middle, and late—that are correlated with Sets W and X and layer z tephras, respectively. The early Kalama phase began with a major dacitic tephra eruption, Wn. Activity continued for several decades and included dacite dome growth, another major dacite tephra (We in 1482), and a number of smaller tephra eruptions and pyroclastic flows. The middle Kalama phase began ~1505 C.E. and included a number of small explosive events (andesitic pyroclastic flows and Set X tephras), lava flows, and lahars. These were followed by eruption of an extensive set of andesite lava flows (Worm Complex and related lava flows) probably around 1545–1550 C.E. The late Kalama phase saw the growth of a large andesite/dacite Summit Dome that formed the upper part of the volcano prior to 1980. Growth of the Summit Dome probably began ~1650 and, during its formation, abundant lithic pyroclastic material and lahar deposits were emplaced on the flanks of the volcano. Magmatic growth probably ended by ~1725, but some flanks of the volcano experienced continued lahar activity as late as 1885 (Yamaguchi and Hobblit, 1995).

The Goat Rocks period includes eruption of dacitic Set T tephra in 1800, emplacement of the Floating Island andesite lava flow, in 1801, and growth of the Goat Rocks dome from ~1830 to 1857. In conjunction with emplacement of the Goat Rocks dome, repeated small hot collapse events built a large fan of lithic pyroclastic material.

The modern eruptive period includes the precursory, pyroclastic, and dome-building events between 1980 and 2008. Phreatic precursory activity began in March 1980. The debris avalanche of May 18 triggered the lateral-blast Plinian eruption of that day. Between May and October, smaller pyroclastic eruptions destroyed incipient domes, emplaced pyroclastic flows on the crater floor and Pumice Plain, and generated minor lahars. Between 1980 and 1986, a composite dome formed on the crater floor, and renewed activity between 2004 and 2008 formed a second composite dome between the 1980–86 dome and the south crater wall.

# Pre-Pumice Plain Field Trip Stop

On our way to Windy Ridge we will stop to explore a few of the pre-1980 eruptive products at Stratigraphy Viewpoint.

## Day 1: From Portland, Oregon, to Stratigraphy Viewpoint Stop (Driving; fig. 1)

The road log is in miles, consistent with signage in the United States. The hiking log is in kilometers to be consistent with units of scientific research.

Note: Mount St. Helens National Volcanic Monument provides a map showing National Forest Roads, trails, and amenities (see fig. 2). It can be downloaded at http://www.fs.usda.gov/main/giffordpinchot/maps-pubs; choose Mount St. Helens overview map.

- From Portland, take Interstate 5 (I–5) north into Washington.
- Take Exit 21 for Washington Highway (Hwy) 503 east toward Woodland and Cougar.
- Turn right onto Hwy 503 south (Lewis River Rd.)
- In 31.6 miles, continue onto National Forest Road NF–90.
- Drive 3.2 miles, and then turn left onto NF–83.
- Continue driving on NF–83 for 10.9 miles, and then park at parking lot on left (just before the bridge crossing the Muddy River).

### Stratigraphy Viewpoint—Description, Stratigraphy, Ages, and Importance

The following text is adapted and modified from Clynne (2003). At this stop we will walk across the Muddy River channel to see a section of pyroclastic deposits that were exposed by a lahar generated by the 1980 eruption. The ages and types of deposits are schematically depicted in figure 3*A*. This outcrop exposes a nearly 16,000-year record of the eruptive history of Mount St. Helens (fig. 3; from Doukas, 1990). Layers include deposits from lahars and dilute pyroclastic currents, alternating with deposits from concentrated pyroclastic currents, fallout tephra, and lava flows that traveled down the Muddy River-Pine Creek fan (for more details, see Mullineaux, 1986, 1996). Note that this river-bank exposure is affected annually by winter floods and the quality of the exposure varies from year to year.

The lahar area is underlain by a fan of Pine Creek age lithic pyroclastic flows. The Muddy River two pyroxene andesite lava

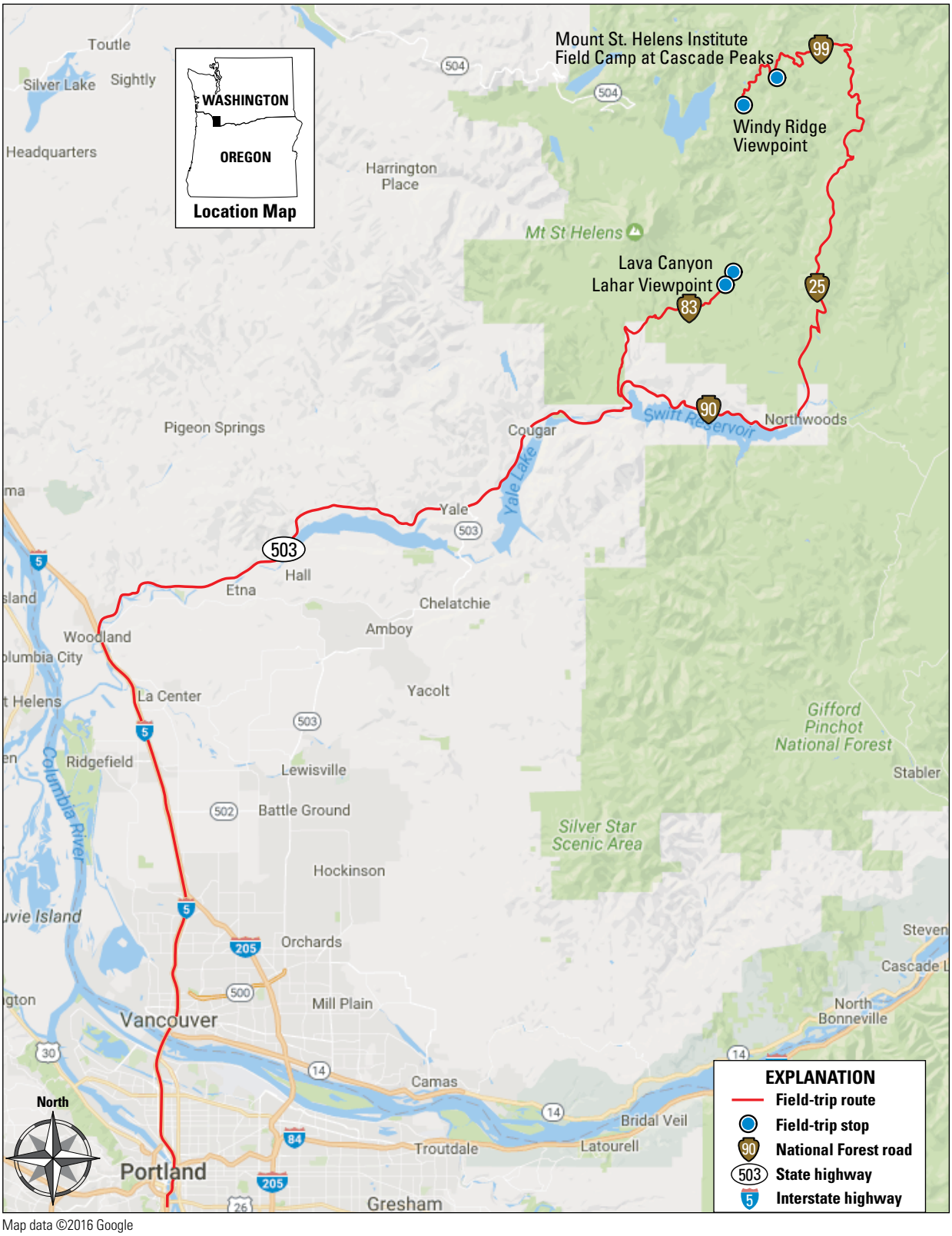


Map data ©2016 Google

**Figure 1.** Map showing route from Portland, Oregon, to Mount St. Helens Institute Campground at Cascade Peak turnout, within the Mount St. Helens National Volcanic Monument, Washington.

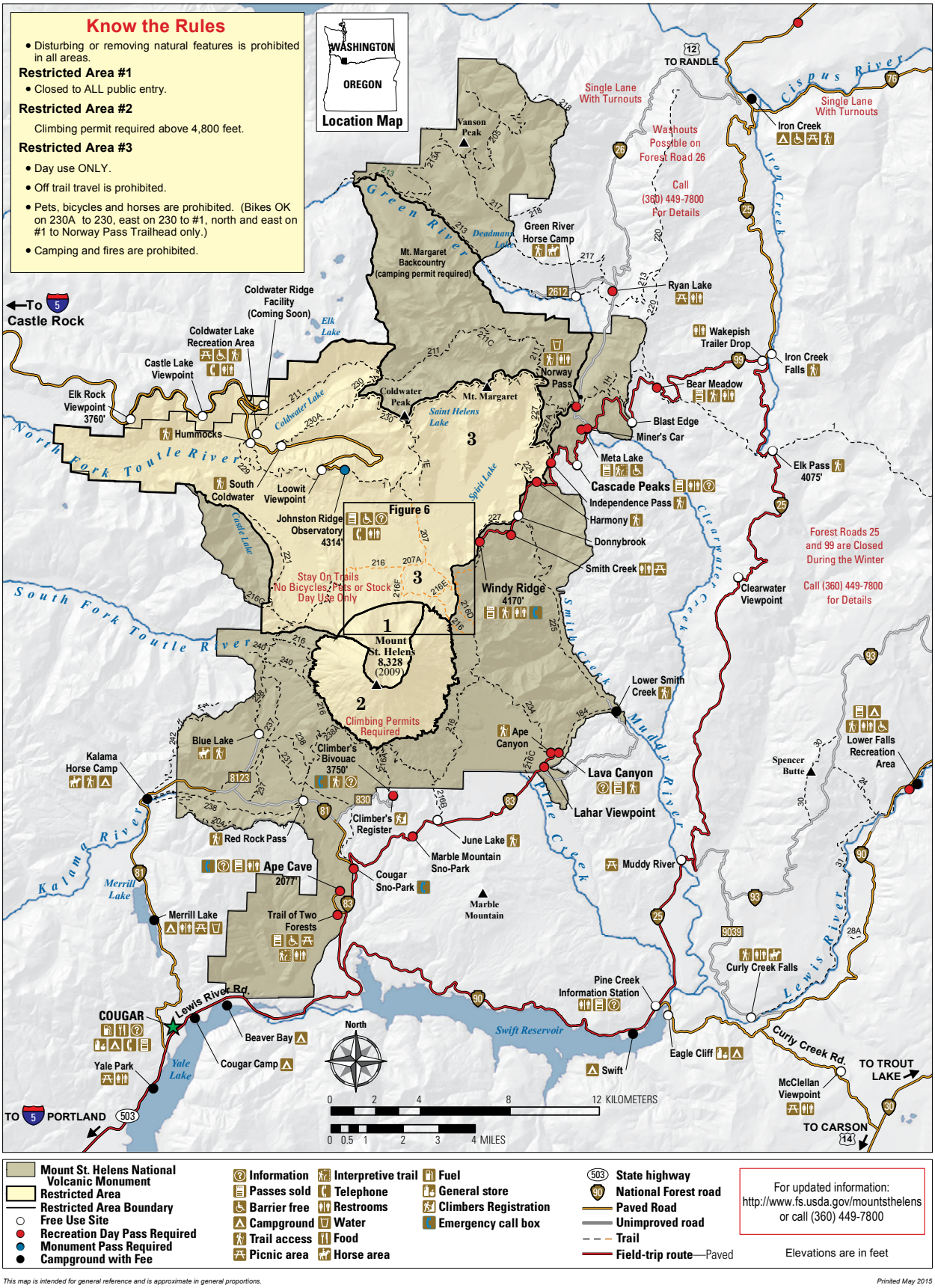


**Figure 2.** Map of Mount St. Helens area, modified from U.S. Forest Service, Mount St. Helens National Monument overview map (https://www.fs.usda.gov/Internet/FSE_DOCUMENTS/stelprd3843447.pdf).

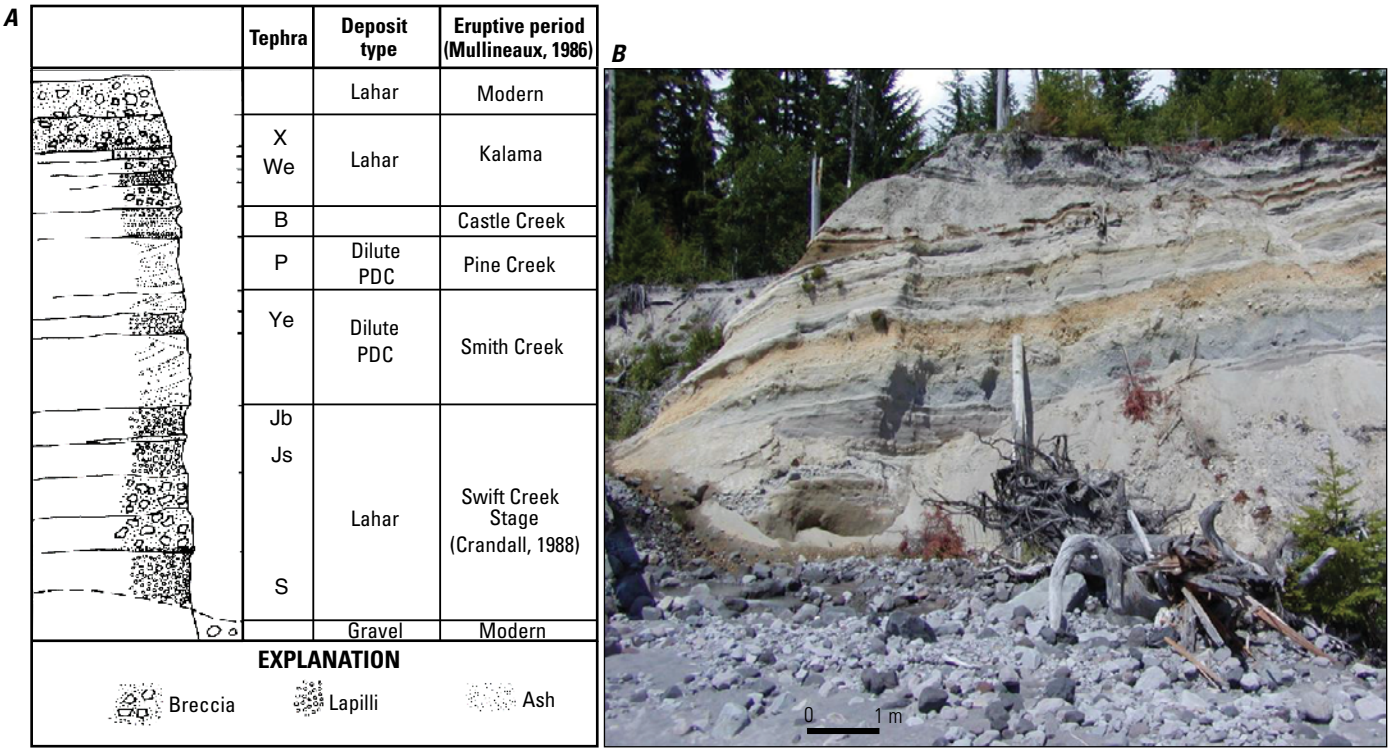


**Figure 3.** Generalized stratigraphic section (*A*) of outcrop (*B*) at Stratigraphy Viewpoint showing nearly 16,000 years of eruptive history of Mount St. Helens (modified from Doukas, 1990). PDC, pyroclastic density current.

flow overlies the Pine Creek deposits and is also exposed in the river bank. The Muddy Creek andesite contains about 59 weight percent $SiO_2$ and contains large, nearly unzoned equilibrium phenocrysts. It has a Pine Creek paleomagnetic direction and is lumped as one of the late (2,550 year old) Pine Creek andesites.

Before 1980, the surface was composed of late Kalama lahars. In this area, the Kalama lahars contain the same Mount St. Helens lithologies (rock types) as the 1980 lahar and can be distinguished only by the presence of 1980 pumice in the young deposit and the lack of older vegetation growing on it. However, this distinction must be made with caution, because 1980 fallout pumice is also present on the surface of both the older and younger lahars.

## Day 1: From Stratigraphy Viewpoint to the Mount St. Helens Institute Field Camp at Cascade Peaks (Driving; figs. 1 and 2)

- Drive southwest (back the way we came) on NF–83 back to NF–90 (10.9 miles [mi]).
- Turn left on NF–90, and drive for 36.9 mi to NF–99. (Note that NF–90 turns into NF–25 at the Pine Creek Information Station; fig.1)
- Turn left on NF–99, and drive 10.5 mi to the Cascade Peak parking lot.
- Accompany field trip leader to the Mount St. Helens Institute Field Camp, which is behind a locked gate (fig. 1).

# Events of May 18, 1980

The May 18, 1980, eruption of Mount St. Helens began at 08:32 local time with collapse of the north flank, which resulted in the largest debris avalanche in recorded history (2.5 $km^3$; details in Criswell, 1987). The debris avalanche deposited decameter-sized hummocks across much of the pumice plain (fig. 4) and as far as 23 km down the Toutle River.

The debris avalanche was immediately followed by the lateral blast, triggered by rapid decompression and expansion of gas within the cryptodome beneath the collapsed edifice (Kieffer, 1981; Fisher, 1990). The lateral blast deposited pumice up to 20 km north of the volcano, destroying 600 $km^2$ of land and old growth forests. The crater and north side of Mount St. Helens were reshaped and eroded down to bedrock by the initial debris avalanche and lateral blast (Christiansen and Peterson, 1981; Rowley and others, 1985).

A Plinian eruption commenced shortly thereafter, with an eruption column that reached 18 km into the atmosphere (fig. 4*A*). About 12:15, ~4 hours into the eruption, the column began to collapse, generating PDCs that traveled northward through the breach (Phase III of Criswell, 1987; fig. 4*B*).

A

B

C

| Eruptive phases | Time, in hours | Eruptive style |
|---|---|---|
| I | 08:32–09:00 | Massive landslide followed by lateral blast |
| II | 09:00–12:15 | Early Plinian |
| III | 12:15–15:00 | Early PDCs |
| IV | 15:00–17:15 | Middle PDCs (Climactic phase) |
| V | 17:15–18:15 | Late PDCs |
| VI | 18:15–May 19th, 1980 | Post eruption phase |

D

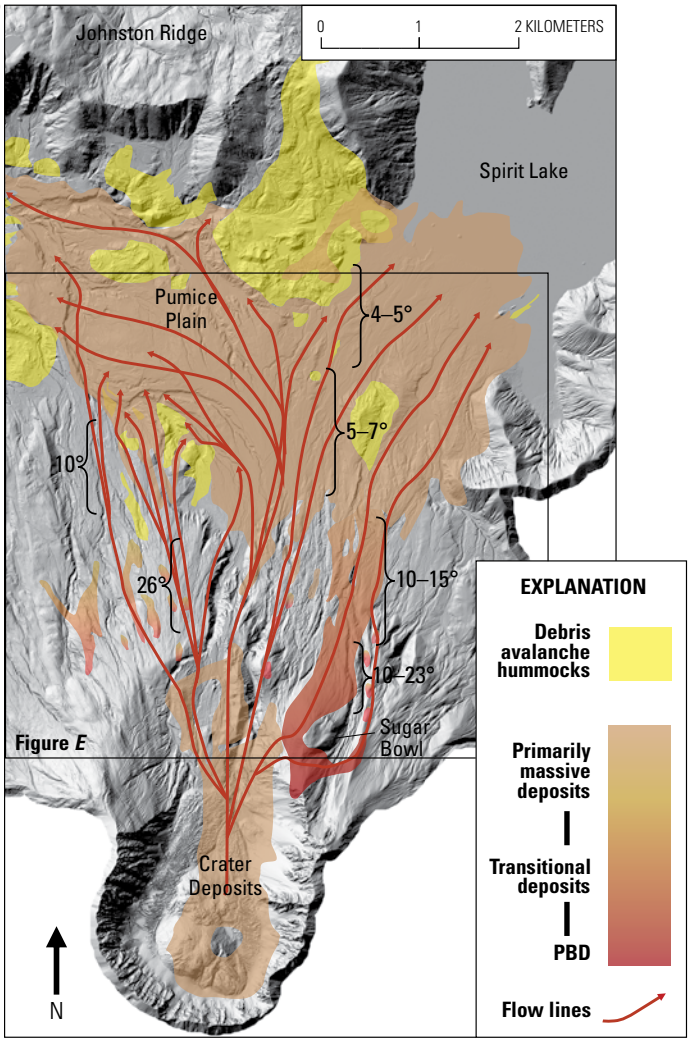


E

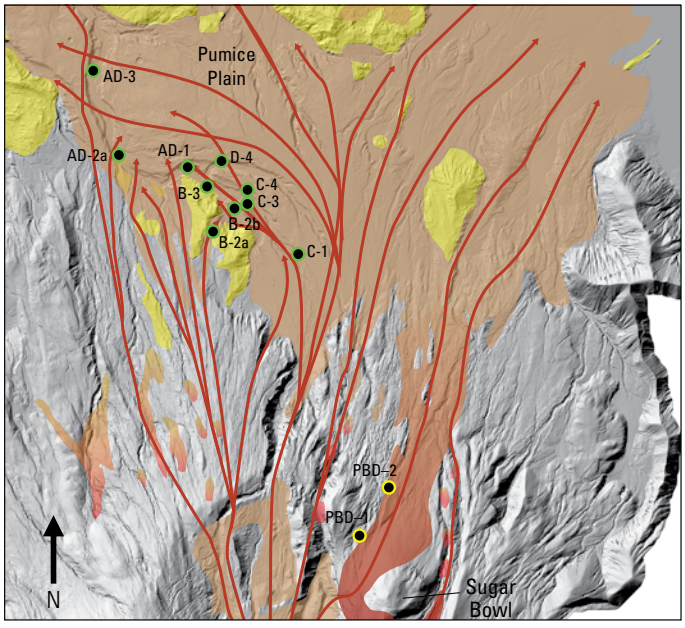


**Figure 4.** *A*, Photograph showing view to north of Plinian eruption column, May 18, 1980, eruption of Mount St. Helens. *B*, Photograph of Plinian eruption column collapsing to the north about 15:50 Pacific Standard Time. *C*, Sequence of events on May 18,1980, highlighting the afternoon pyroclastic density currents (PDCs) deposited throughout the pumice plain (Criswell, 1987). *D*, Lidar map of the Mount St. Helens crater north through the pumice plain, with overlay showing interpreted flow paths and slopes of the topography (modified from Rowley and others, 1985). PDB, proximal bedded deposits. *E*, Enlarged lidar map of pumice plain showing outcrop names and locations. See *D* for map location. Photo *A* by Robert Krimmel and photo *B* by Joseph G. Rosenbaum; both photos are public images provided by the Cascade Volcano Observatory, U.S. Geological Survey.

PDCs became more voluminous through Phases III and IV of the eruption, and began to wane during Phase V (table 2; fig. 4). PDC deposits are found within the crater (inner crater deposits), along the flanks (proximal bedded deposits or PBD), and throughout the pumice plain (fig. 4*C*) to a maximum distance of 9 km north of the vent. The eruption ended about 18:15 local time. Table 2 gives the sequence of phases and deposits at Mount St. Helens on May 18, 1980, based on previous work.

The original extent of the PBD along the flank, as mapped by Rowley and others (1985), extended 100 m above the post-eruption crater floor along Sugar Bowl dome and down along the east flank, where slopes range from 10 to 30° (figs. 4 and 5). PBD were <6 m thick where found above the crater floor (fig. 5*B*) and up to 20 m thick along the east flank (west of and below Sugar Bowl dome; fig. 5*C*). The PBD transition into the pumice plain deposits along the middle to the base of the flank (figs. 5*D* and 5*E*), where an increase in the size and proportion of lithic clasts was also noted. Small, ≤4-m-thick patches of PBD were also found along the 26° slope west of the breach. The western slope has significantly less surface topographic irregularities (for example, slot canyons) than the flank east of the breach, which Rowley and others (1985) suggest may have influenced the location and rate of deposition.

The thickest deposits from the afternoon PDCs are found throughout the pumice plain (fig. 4*C*) and comprise four primary flow units. These units, found across the entire pumice plain, are briefly described here; a more detailed account can be found in Brand and others (2014).

**Table 2.** Summary of phases during the May 18, 1980, eruption at Mount St. Helens, Washington, with relative timing and duration of the PDCs that flowed north through the breach (modified from Criswell, 1987). Only the voluminous PDCs that traveled through the north breach and across the pumice plain, and the correlated PDC unit, are listed. Column height and mass flux estimates from Carey and others (1990) and Andrews and Gardner (2009). Modified from Brand and others (2014). PDC, pyroclastic density current; N/A, not applicable.

| Phase | Time (hours) | Eruption style | Column height; mass flux (kg/s) | Timing and duration of north breach funneled PDCs | Pumice plain stratigraphic PDC unit |
|---|---|---|---|---|---|
| I | 08:32–09:00 | Massive landslide followed by lateral blast | Not reported | Lateral blast reached maximum distance in 5–7 minutes. | Blast deposits (only found beyond 8.5 km from source, below Johnson Ridge). |
| II | 09:00–12:15 | Early Plinian Phase | 15–18 km; $6.3\times10^6$ to $1.3\times10^7$ kg/s | N/A | N/A |
| III | 12:15–15:00 | Early PDCs | 13–16 km; $3.9\times10^6$ kg/s | 1217—PDC "poured through the breach," generating 4–7 km elongated ash cloud; 13:30–14:00—episodic PDCs emplaced in the upper Toutle Valley (unclear if these reached the pumice plain); 14:30–15:00—size of flows increased. | Units I and II. |
| IV | 15:00–17:15 | Climactic PDCs | 13–16 km; $4.0\times10^7$ kg/s | 1500—"numerous, large" PDCs were observed to spill over the crater rim, engulfing the volcano, reaching spirit lake. PDC flux to the north abated about 16:35. PDC activity that began to wane at 16:05, ceasing at 16:35. | Unit III and possibly Unit IV. |
| V | 17:15–18:15 | Late PDCs | Not reported | Short-lived increase in activity during the waning phase produced a PDC pulse that flowed into the upper Toutle valley at 1745, reaching Spirit Lake at 17:47. A second PDC pulse to the north occurred at 18:10. | Possibly Unit IV and Unit V (latter on surface only; no outcrop exposures). |
| VI | 18:15–May 19, 1980 | Waning and post eruption phase | N/A | N/A | N/A |

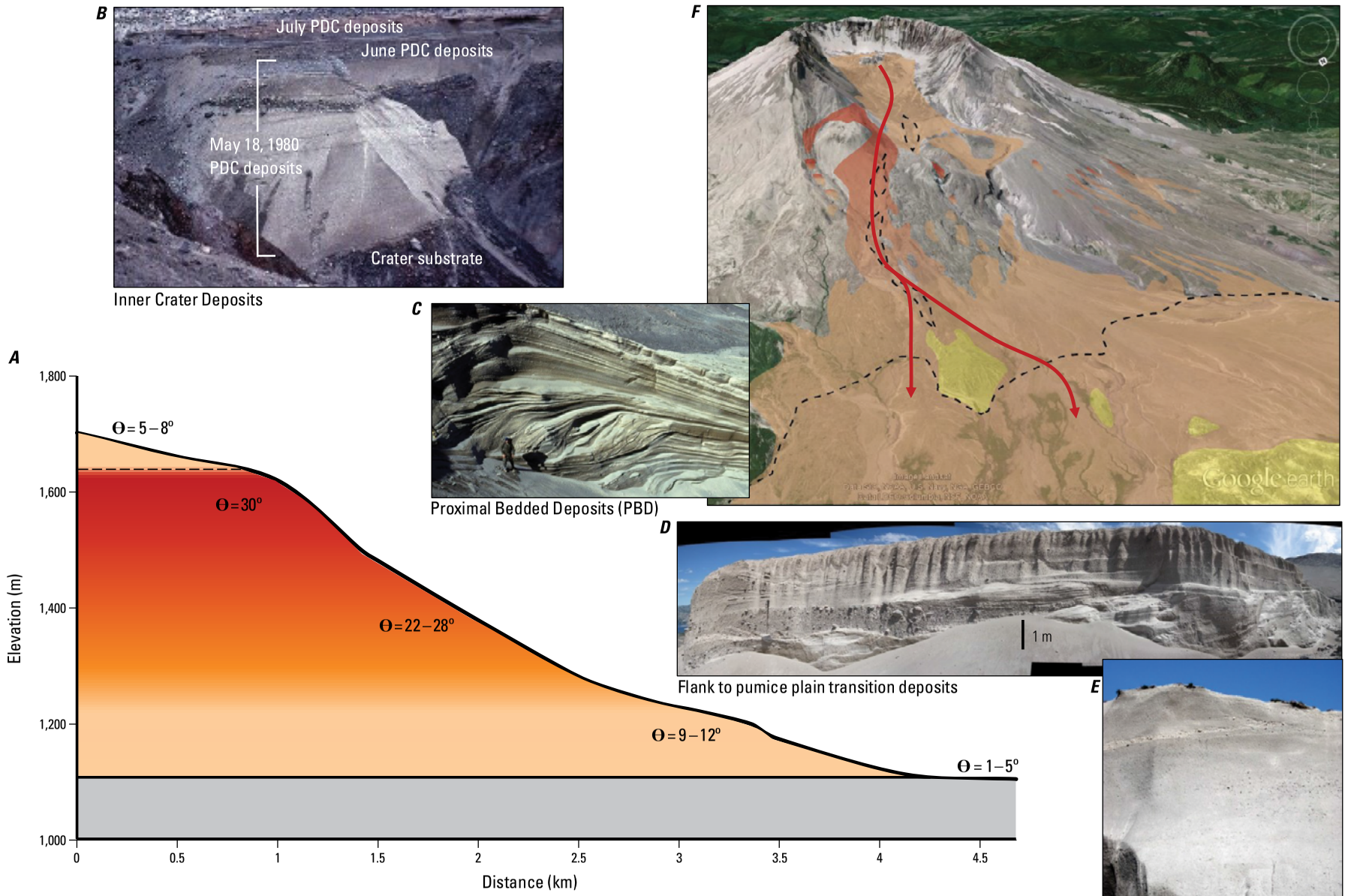


**Figure 5.** Path of May 18, 1980, pyroclastic density current (PDC) that flowed down the east flank of Mount St. Helens, Washington. *A*, Profile of northeast path from the crater down to the pumice plain, illustrating the changes in slope (θ, slope). The color scheme key is in figure 4*D*. *B*, Photograph showing massive PDC deposits exposed in the crater of Mount St. Helens (photo by Steve Self, early 1980s; May 18 deposit, ~3 m thick). *C*, Photograph showing proximal bedded deposits (PDB) found high on the steep (θ, ~25°) flanks. *D*, Photograph showing transitional deposits found on moderate slopes (θ, ~12°). *E*, Photograph showing massive, pumice plain deposits found beyond the break in slope (θ, ~5°). Geologist for scale. *F*, Google Earth image with modified Rowley and others (1985) map overlay. Dashed lines delineate 2015 exposures.

## Terminology and Methods

Lithofacies terminology is adapted from Branney and Kokelaar (2002; table 3). We use the term "sustained" to represent collapse or fountaining of the column over an extended period of time (minutes to tens of minutes). Waxing or waning at the vent during PDC production, and unsteady and variable conditions during transport and deposition of the PDCs, are expected over the duration of sustained PDC activity. F2/F1 represents the fines ratio for PDC deposits; the ratio is used to determine the degree of fines depletion or fines enrichment (where F2 ≤0.0625 mm and F1 ≤1 mm). Following the findings of Brand and others (2014), PDC deposits from the afternoon of the May 18, 1980, eruption with F2/F1 ≤0.1 are fines-depleted, F2/F1 ≤0.15 are fines-poor deposits, F2/F1 between 0.16–0.31 are fines-normal, and F2/F1 ≥0.32 are fines-enriched.

The statistical method of Pollock and others (2016) is used to determine if the PDCs entrained lithic blocks from the paleo-substrate along the steep flanks of the volcano or from the debris avalanche deposits. The method assumes that the lithic population in the coarsest fall deposit from the May 18, 1980, eruption, correlated with the climactic, PDC-producing phase, is an acceptable proxy for the initial distribution of vent-derived clasts during the column-collapse, PDC-generating phase of the eruption. Lithic componentry was completed for the fall deposits and PDC deposits along the flanks and throughout the pumice plain. For each sample, 100 lithic blocks (>64 mm) were collected, identified, and classified into one of the four recent eruptive periods (3 ka–present): Goat Rocks, Kalama, Castle Creek, and Pine Creek (see Hausback 2000, for a description of the lithologies). The average of three sampled fall deposits is used to represent the vent-derived clast population.

**Table 3.** Pyroclastic density current (PDC) facies terminology and abbreviations adopted from Branney and Kokelaar (2002).

| Facies label | Lithofacies |
|---|---|
| mT | Massive tuff. |
| mLT | Massive lapilli tuff. |
| $mLT_f$ | Massive lapilli tuff with fabric. |
| $mLT_{bl}$ | Block-rich massive lapilli tuff. |
| $mLT_{bl-f}$ | Block-rich massive lapilli tuff with fabric. |
| mlBr | Massive lithic breccia. |
| sLT | Stratified lapilli tuff. |
| xsLT | Cross-stratified lapilli tuff. |
| dsLT | Diffuse stratified lapilli tuff. |
| dsBr | Diffuse stratified breccia. |
| dxsLT | Diffusely cross-stratified lapilli tuff. |
| lensP | Pumice lens. |
| lenslBr | Lithic breccia lens. |

The componentry of PDC deposits is compared to that of the fall deposits using the Chi-square test for homogeneity (for example, Eisenhart, 1935). This method determines the statistical likelihood of the PDC lithic population having the same source as the fall deposits (vent erosion) or the likelihood that lithics were entrained from a second source (volcano substrate). A P-value represents the probability of obtaining a higher Chi-square value than the one calculated, if both samples are derived from the same parent population (see Pollock and others, 2016, for method details). A significance level of 0.05 distinguishes between samples that are likely to contain locally entrained blocks and those that do not. P-values >0.05 indicate that the distribution of lithic lithologies in the PDC sample is consistent with only those derived from vent erosion. P-values <0.05 indicate that the population of lithics in the PDC sample consists of both vent-derived clasts and locally entrained clasts from the substrate.

## Mount St. Helens PDC Flow Units

The descriptions in this section are adapted from Brand and others (2014, 2016) and Mackaman-Lofland and others (2014). Figure 6 shows locations of each outcrop and field stop.

Units I and II are correlated with the first voluminous PDCs generated during eruptive Phase III, when PDCs "poured through the breach" (table 2; fig. 4; Criswell, 1987), and are interpreted to have filled in and around the debris avalanche hummocks scattered across the pumice plain. In proximal regions, both Units I and II are dominantly diffusely stratified and (or) diffusely cross-stratified lapilli tuff, suggesting transport and deposition under highly unsteady conditions where basal conditions varied from low to somewhat higher basal shear stress, resulting in periods of traction transport and (or) granular flow boundary conditions. Evidence for traction transport is interpreted as a consequence of variability in surface roughness and irregularities and in unsteadiness within the currents. In contrast, the distal deposits of Units I and II are dominated by massive lapilli tuff, suggesting a shift to more concentrated conditions with lower boundary shear stress (relative to upstream current conditions). The change in conditions is interpreted as the result of current compaction due to increased sedimentation with distance from source.

Units I and II thicken with distance from the source, suggesting portions of the currents bypassed more proximal locations to deposit the bulk of the sediment distally. Pumice lenses are common in both units and increase in size and abundance distally, suggesting efficient segregation processes within the aggrading currents. Units I and II are largely fines-depleted up to 6 km from the source and fines-normal to fines-enriched to their distal exposures up to 8 km from the source. The fines pattern suggests elutriation was a dominant process across much of the depositional region, but fines became progressively trapped in the basal portions of the currents as flows compacted during transport. Pumices within the deposits are completely rounded within a kilometer of the base of the volcano; thus, ash added by comminution is considered negligible for the increase in fines with distance from the source (compare with Dufek and Manga, 2008).

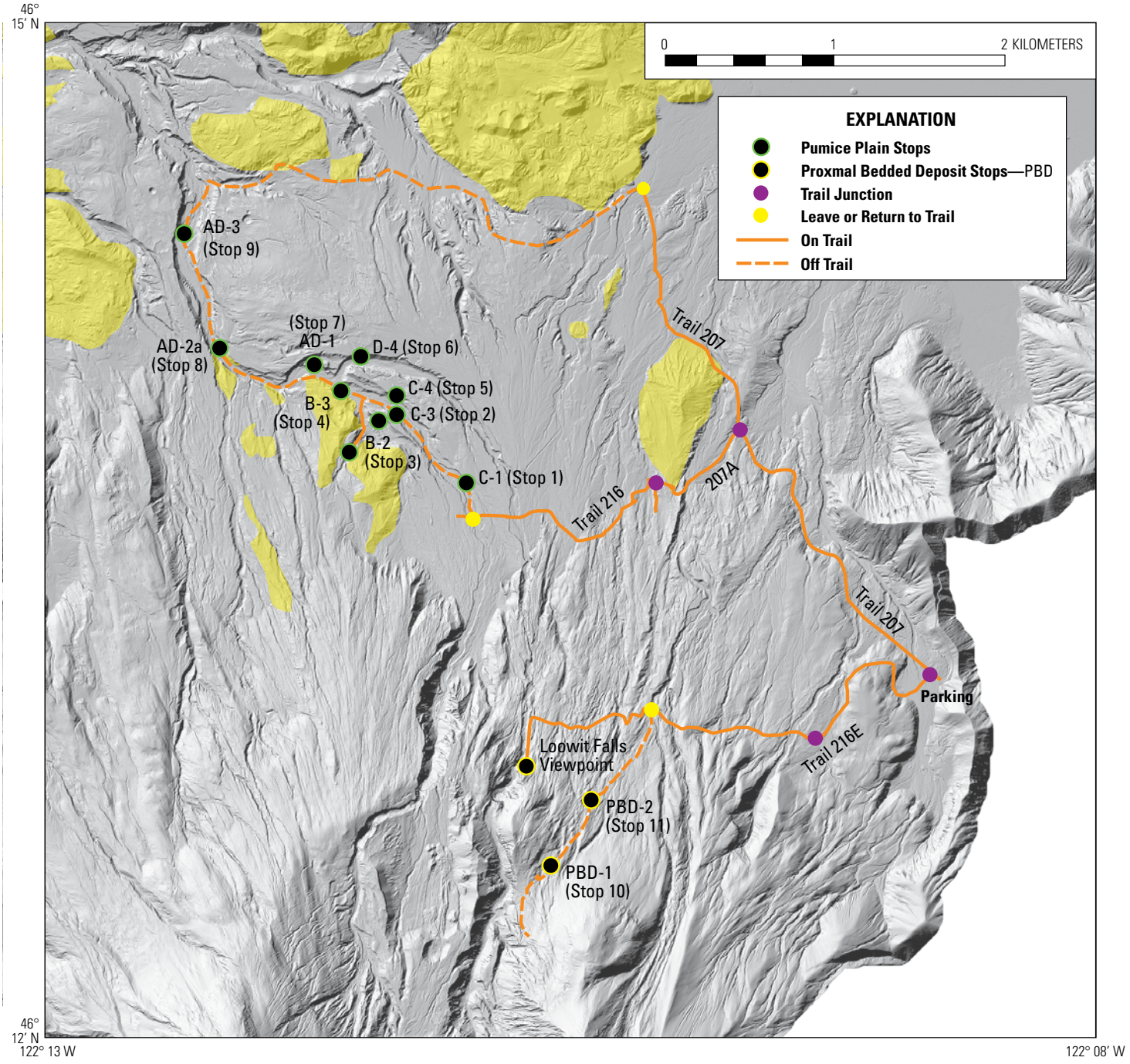


**Figure 6.** Map showing hiking route and locations of Stops 1–11 on the pumice plain, Mount St. Helens, Washington. UTM coordinates for each stop are available in table 4. Drainages are named alphabetically from west (A) to east (J). Only drainages B, C, D, and AD (past the junction of drainages A and D) will be visited on this trip, along with two proximal bedded deposits (PBDs). Shaded-relief base from https://pubs.er.usgs.gov/publication/ds904.

PDC Units III and IV are correlated with the climactic, most voluminous phase of the eruption (Phase IV, table 2), where "numerous, large" PDCs were observed to spill over the crater rim, engulfing the volcano and reaching Spirit Lake (Criswell, 1987). Both flow units are composed of lithic tuff breccias, lithic block-rich massive lapilli tuffs, and massive lapilli tuff (figs. 7 and 8). Lithic blocks are primarily derived from crater widening and entrainment of clasts from the debris avalanche hummocks across the pumice plain (Pollock and others, 2016), suggesting the flows traveled up and over topography, as well as between debris avalanche hummocks. Deposits of Units III and IV are also mapped along and beyond the west flank of the volcano, suggesting the currents took multiple flow paths from the initiation of column collapse (breach and flanks).

The pronounced lithic breccias found at the base of the flow unit boundary in Unit III suggest segregation of the block-sized accidental lithic clasts (referred to simply as lithics, hereafter). However, weak to negligible apparent fabric, dominantly fines-normal to fines-enriched deposits, and weak evidence for pumice or ash segregation (for example, lack of pumice lenses) in Unit III suggest mLT was transported and deposited from a highly concentrated, fluidized current with suppressed size-density segregation (compare with Druitt, 1995; Druitt and others, 2007). In contrast, the massive nature of Unit IV, accumulation of lithic blocks at the basal flow boundary, fines-depletion up to medial locations (up to 5.3 km), and abundant pumice lenses suggest transport and deposition from a concentrated, fluidized current where size-density segregation occurred. Evidence for size-density segregation suggests a current that was less concentrated relative to the PDCs responsible for Unit III.

# Start of Road and Trail Log with Stop Descriptions

## Day 2 (Stops 1–4) and Day 3 (Stops 5–9):

**Mount St. Helens Institute Field Camp to Trailhead (Driving, Hiking)**

- From Cascade Peak parking lot, turn left on NF–99 and drive 5.6 mi to the Windy Ridge Viewpoint parking lot (fig. 1). We will pass through the (locked) gate on the south side of the parking lot.
- After passing through the gate, we will drive 2.0 mi down a gravel path to the main trailhead at the base of the ridge (gravel road is marked as Trail 207 on the National Forest Service trail maps).

**Trail log changes from driving (miles) to hiking (kilometers)**

- Continue on foot along Trail 207 for 2.3 kilometers (km).
- Turn left at the junction onto Trail 207A (fig. 6).
- Hike 1.4 km, then turn right on Trail 216 at the next junction.
- Hike for 0.6 km and stop along the trail.
- Turn north to hike down the drainage (drainage C of Brand and others, 2014); continue 0.3 km to outcrop C-1.

**Notes**

- Coordinates for all stop locations are found in table 4.
- Outcrop exposures are affected annually by erosion, and the quality of the exposure varies from year to year.

**Table 4.** Outcrop locations and distance from center of crater, Mount St. Helens, Washington. Distance based on interpretation of flow path is also approximated from center of crater.

| Outcrop (fig. 5) | UTM east (E.)[1] | UTM north (N.)[1] | Linear distance from crater center (km) | Distance based on interpretation of flow path (km) |
|---|---|---|---|---|
| PBD-Proximal | 563482.7 | 5118944. 5 | 2.8 | 2.7 (along eastern flank) |
| PBD-Transitional | 563662.6 | 5119181.6 | 3.2 | 3.2 (along eastern flank) |
| C-1 | 562715.5 | 5121085 | 4.8 | 4.8 (through breach) |
| C-3 | 562315 | 5121415 | 4.9 | 5.1 (through breach) |
| B-2b | 562085 | 5121310 | 4.9 | 4.9 (along western flank) |
| B-2a | 562166 | 5121454 | 5.0 | 5.2 (along western flank)<br>5.3 (through breach) |
| C-4 | 562255 | 5121589 | 5.0 | 5.2 (through breach) |
| D-4 | 561987 | 5121706 | 5.3 | 5.4 (through breach) |
| B-3 | 561931.6 | 5121584.8 | 5.3 | 5.4 (through breach) |
| AD-1 | 561906.6 | 5121691 | 5.3 | 5.2 (along western flank)<br>5.5 (through breach) |
| AD-2a | 561209.2 | 5121813 | 5.6 | 5.4 (along western flank)<br>6.36 (through breach) |
| AD-3 | 560984.9 | 5122402 | 6.5 | 7.25 (through breach) |

[1]UTM Zone 10T

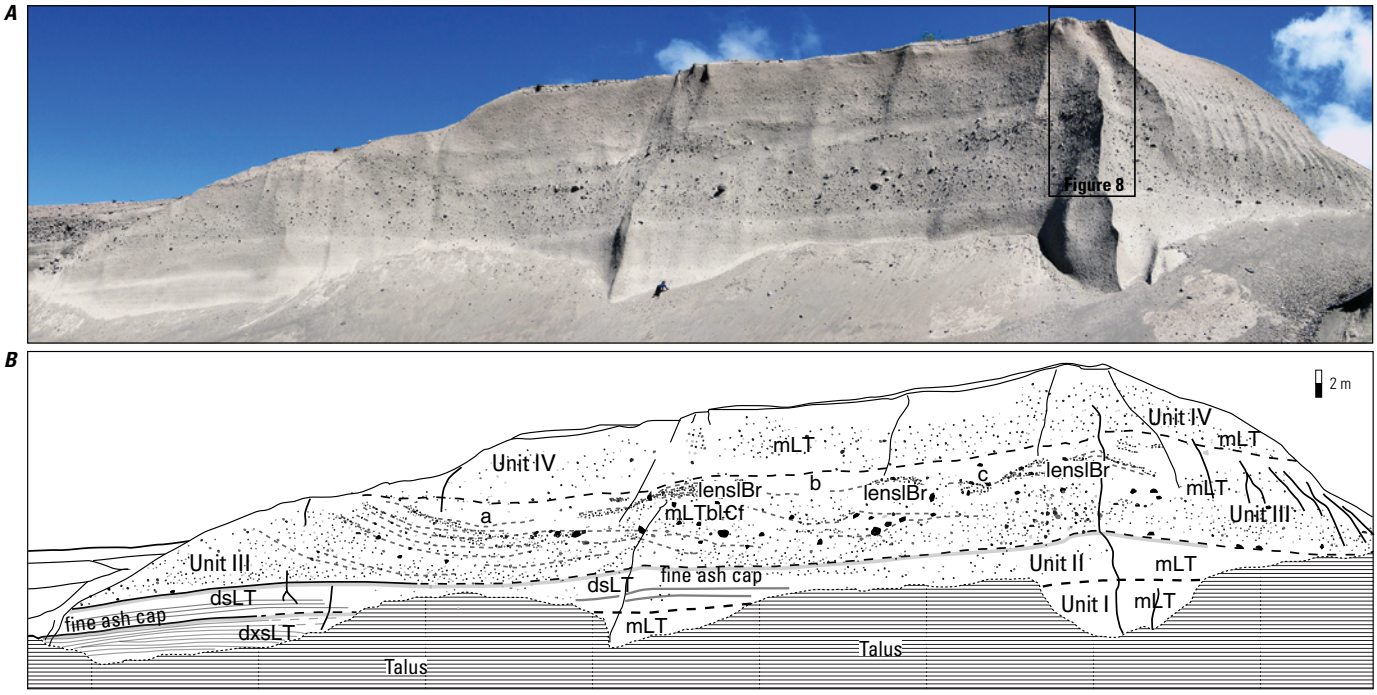


**Figure 7.** *A*, Photograph showing exposure of the east side of the AD-1 outcrop (see fig. 6 for location). Geologist is 1.5 m for scale. *B*, Labeled sketch of AD-1 outcrop; see tables 1–3 for label explanations. Thick solid lines represent unit contacts. Thin dashed lines represent apparent imbrication, based on the long-axis orientation of blocks (please note, lines do not represent stratification). *C*, Photograph showing close-up view of Units I and II and the interpreted co-ignimbrite ash that caps them (Unit III).

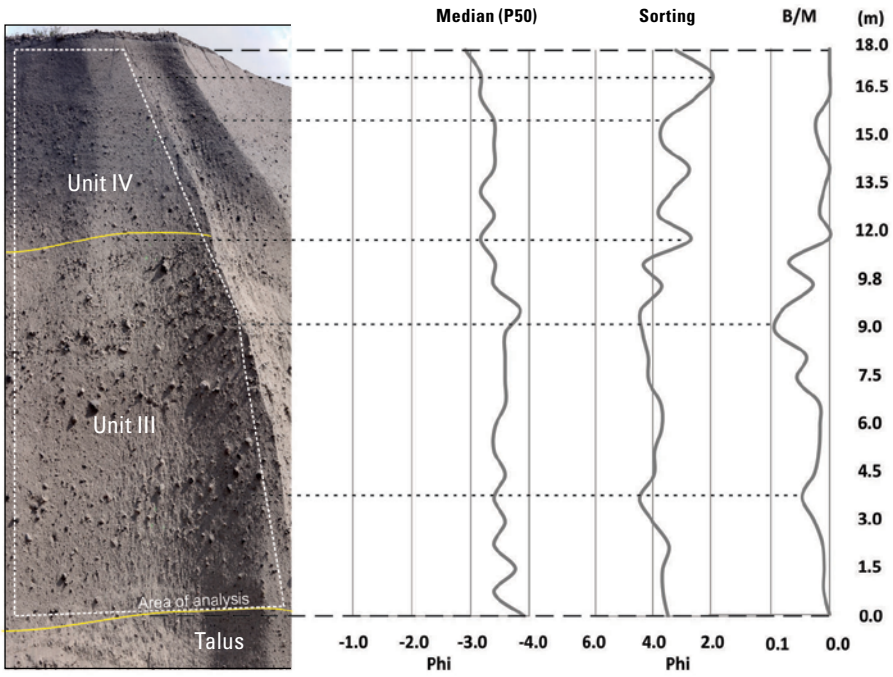


**Figure 8.** Vertical granulometric profiles of median (P50), sorting, and block-to-matrix (B/M) ratio for units shown in photograph. The curves are obtained using Laser Remote Optical Granulometry (LROG). The method provides quantitative granulometric patterns through tens of measurements along a vertical profile. For method details, see Sarocchi and others (2005) and Moreno-Chavez and others (2015).

## Stop 1: Outcrop C-1

Outcrop C-1 is located 4.8 km from the vent and cut parallel to flow direction (fig. 9). The base of the exposed Unit IV sequence at outcrop C-1 begins with a fines-depleted basal mlBr (table 3), which grades vertically and laterally into fines-depleted dsLT to mLT. Blocks range from 0.64 to 1.2 m in their longest dimension and are composed of accidental lithics including basalt, andesite, dacite, and rhyodacite. Weak imbrication is observed; the long axes of the blocks are roughly parallel to the inferred depositional surface. The block-rich region is 3.5 m at its thickest (the base is not exposed at this location) and is 23 m in length. The blocks decrease in size vertically and splay at an upward, 15° angle in the downstream direction before diffusing into dsLT to mLT. The basal mlBr grades vertically and laterally into dsLT and mLT.

The breccia at the base of the sequence suggests deposition from a density-stratified PDC that segregated dense blocks toward the base of the current (for example, Macías and others, 1998; Branney and Kokelaar, 2002). Lithic lithology indicates the vent as the primary source of the accidental lithic clasts (fig. 9). The massive, fines-depleted nature of the breccia suggests deposition from a fluid-escape-dominated flow boundary. However, the weak fabric suggests some influence of flow-boundary shear stress within the basal region of the current (Branney and Kokelaar, 2002). The massive nature of the surrounding mLT suggests deposition by a concentrated flow, with rapid deposition and relatively lower boundary shear stress. The fines-poor nature of mLT suggests that elutriation was efficient and, thus, that sedimentation fluidization was an important particle-support mechanism in the depositional region of the current.

## Stop 2: Outcrop C-3

Outcrop C-3 is located 0.5 km downstream from outcrop C-1. Flow direction for this outcrop is left to right; the exposed deposits are mapped as Unit III, although the lack of continuous exposure prevents conclusive identification of the flow unit. Facies within the outcrop vary from mLT to mLTbl. A striking, downstream-elongated, wave-like structure was exposed for the first time during the summer of 2016 (fig. 10*A*). Here, the mLTbl is bounded by mLT, with the wave-like feature extending and fading into the mLT. We interpret the feature as a shear-induced flame structure, similar to the lab-created structures of Rowley and others. (2011).

## Stop 3: Outcrop B-2

Outcrop B-2 is on the backside of outcrop C-3. Flow direction for this outcrop is right to left; the exposed deposits are mapped as Unit III, although the lack of continuous exposure prevents conclusive identification of the flow unit. We see several stacked lithic breccia layers (fig. 10*B*); the bottom breccia is ungraded to weakly reverse graded, while the upper 2–3 layers are distinctly reverse graded and diffusely stratified (dsBr). The

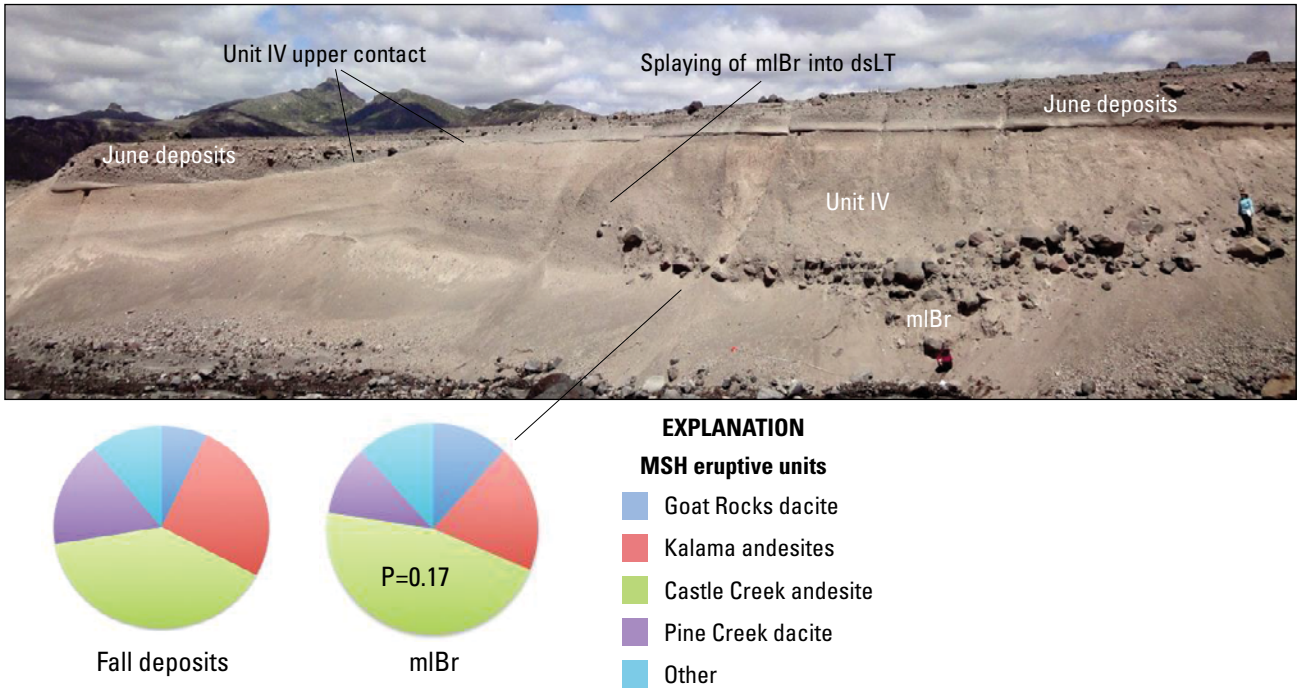


**Figure 9.** Photograph showing outcrop C-1 (Stop 1; see fig. 6 for location), which is located 4.8 km north of the vent and includes the lithic-rich base of Unit IV (pie charts represent componentry). The componentry has a P-value of 0.17, indicating most lithic blocks were eroded from the vent and not the steep flanks. Geologist for scale.

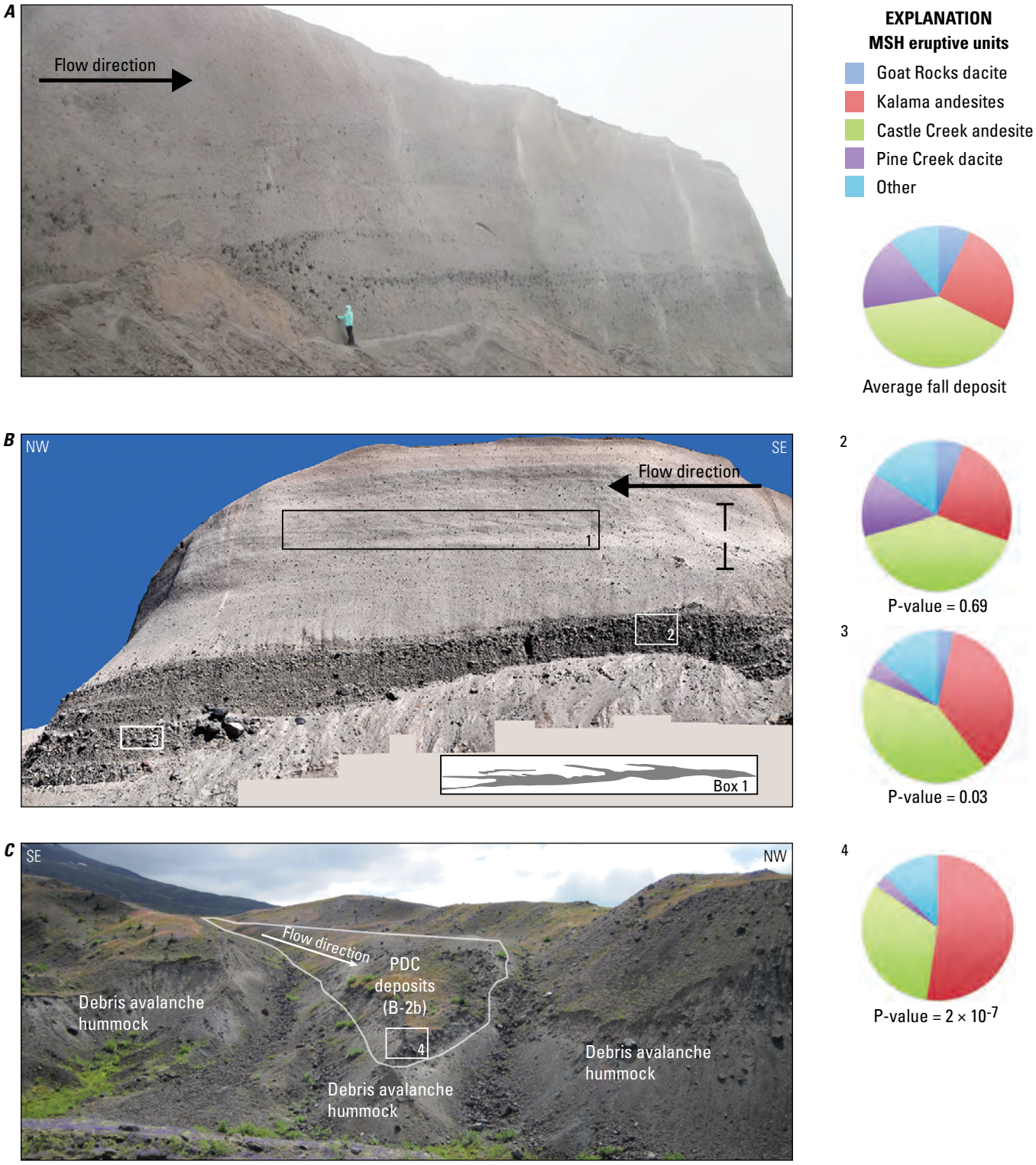


**Figure 10.** *A*, Photograph of outcrop C-3 (Stop 2; see fig. 6 for outcrop locations) showing a striking, downstream-elongated, block-rich feature extending and fading into mLT. The feature is interpreted to be a shear-induced wave-like structure similar to those produced by the experiments of Rowley and others (2011). Geologist for scale. *B*, Photograph showing outcrop B-2a (Stop 3), a series of lithic breccia layers overlain by mLT. The lithic breccias are reverse graded and the componentry suggests that the majority of lithics are vent derived. This outcrop also contains similar wave-like structures (sketched in Box 1) to those found in outcrop C-3. *C*, Photograph of view looking to the southwest from outcrop B-2a (Stop 3). Pyroclastic density current (PDC) deposits fill a paleo-valley formed between two large debris-avalanche hummocks (outcrop B-2b; Stop 3). Boxes labeled 2–4 in photographs *B* and *C* represent sample locations. Pie charts represent sample componentry; each sample number corresponds to a numbered box in the images. The componentry of the PDC deposits suggests a high proportion of locally entrained lithic blocks from the debris-avalanche deposits.

breccias are bounded by mLT. The upper breccia grades into overlying mLT, with individual or trains of coarse lapilli and block lithics dispersed within the first 0.5 m. Although faint, a series of downstream-elongated wave-like structures, similar to the one at outcrop C-3 but smaller, tighter, and within mLT, are exposed higher in the section (Box 1, fig. 10*B*). These features are also interpreted to represent shearing at the flow-boundary interface as the PDC deposits aggraded.

Several large hummocks and debris-avalanche deposits are exposed just to the southeast of outcrop B-2a. A small, paleovalley is filled with PDC deposits (outcrop B-2b), interpreted to have flowed down the west flank and between the hummocks. Componentry of the PDC deposits, just above the debris avalanche contact, indicate significant local erosion (P-value of $2 \times 10^{-7}$). While it is possible that the lower-most, primarily massive breccia at outcrop B-2a was derived from the paleovalley to the southeast, the stratification, grain alignment, and higher P-value of the upper breccia(s) (P-value = 0.69, consistent with a vent-derived source) in outcrop B-2a indicate a flow direction perpendicular to the paleovalley. Thus, it is unclear if the flows down the paleovalley collided with the currents that traveled through the main breach or if they stopped short of the outcrop exposure.

## Stop 4: Outcrop B-3

- Hike 1 km down the drainage to outcrop B-3.

Outcrop B-3 is located 5.22 km from the vent and directly adjacent to a set of large (>50 m tall) debris-avalanche hummocks (fig. 6). The outcrop is oriented roughly N. 60° W., somewhat parallel to flow direction. A massive, block-rich, debris-avalanche hummock is exposed at the base of the outcrop (fig. 11). The contact between the hummock and overlying PDC deposits is angular and dips 25–35° to the northeast, implying a wedge-shaped geometry of the PDC deposits against the side of

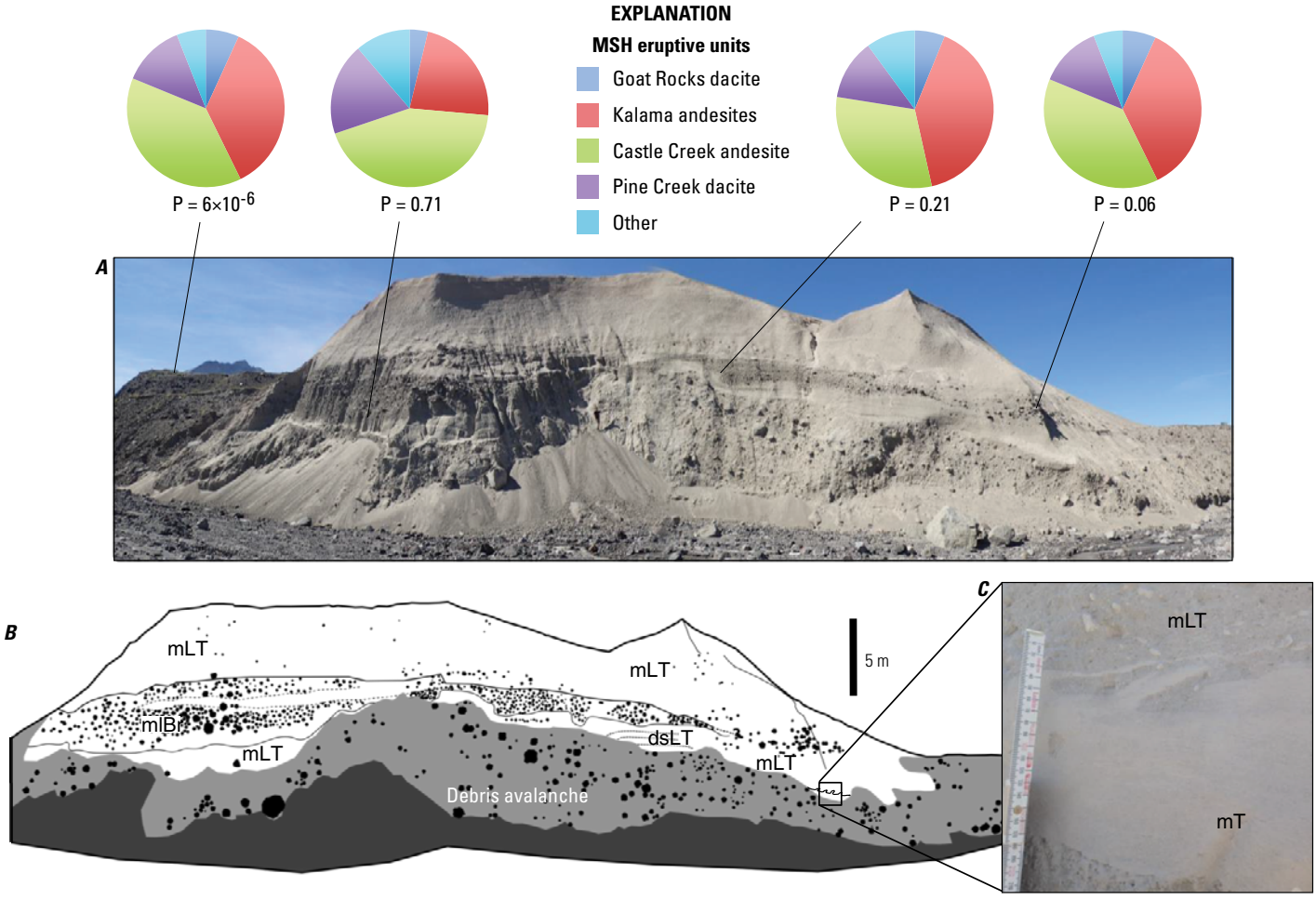


**Figure 11.** *A*, Photograph of outcrop B-3 looking to the west. Pie charts show componentry of different samples taken from the outcrop; P-values indicate lithic blocks within the pyroclastic-density-current (PDC) deposits are vent derived. *B*, Labeled sketch of outcrop B-3. *C*, Close-up photograph of wave-like feature interpreted as a shear-induced mixing structure.

the hummock. As exposed, the contact between the hummock and PDC deposits undulates (contact between gray and white units in fig. 11), with troughs spaced ~2–3 m apart.

A thin (<10 cm thick), fine-grained, well-sorted massive tuff (facies mT) is found within some of the troughs. The source of the ash is unresolved but may be related to reworked co-ignimbrite ash from the lateral blast. The dissimilarity of mT relative to the underlying debris avalanche and overlying mLT deposits further suggests that mT was deposited after emplacement of the hummocks and before the beginning of the PDC-producing eruptive phase.

The PDC deposits begin with a relatively continuous mLT to dsLT transition that varies in thickness from 3 m to only a few centimeters, where it pinches out along higher points of the debris avalanche hummock (fig. 11). The contact between the mT in the troughs and the overlying mLT is characterized by shear-induced flame structures (elongated in the interpreted downstream direction) that extend to the northwest (fig. 11*C*). The contact between the mLT and the debris-avalanche hummock elsewhere is sharp.

The mLT has a gradational contact with overlying mlBr. The mlBr on the south side of the outcrop is 5 m thick, reverse graded, and predominately clast supported and contains blocks up to 1.6 m in diameter. Lenses of mLT can be found within mlBr. To the north, the mlBr layer thins to <1 m; it is laterally discontinuous up to 15 m to the north, has a wavy appearance, and has fabric bordering on diffuse stratification due to coarse grain alignment ($mlBr_f$). The contact between $mlBr_f$ and the uppermost mLT is gradational. The mLT layer is up to 6 m thick, continuous across the entire outcrop, and contains occasional blocks up to ~10 cm in diameter.

Componentry of lithic-rich mlBr indicates the blocks were primarily derived from the vent (fig. 10). Diffuse stratification in the lower mLT region suggests high shear at the base of the current, possibly enhanced by the irregular topography of the debris-avalanche contact. Shear is further noted by the flame structures along the contact of mT and mLT (fig. 11*C*), suggesting a primary flow direction along the same strike as the outcrop. The high proportion of blocks suggests the exposure contains deposits from Unit III; however, direct correlation with a distinct unit is not possible in this location due to lack of continuous exposure.

## Day 3: Stop 5, Outcrop C-4

We will return 0.3 km up the drainage (almost directly east of outcrop B-3) to view outcrop C-4. The outcrop is ~5.3 km from the source. Two convex breccia lenses are exposed along the outcrop, interpreted as Unit IV due to the contact with the later June flows (fig. 12*A*). The entire feature is ~58.5 m across; the wavelength of the western convex breccia is 27.5 m, and the eastern convex breccia is 31 m. A potential third convex lithic breccia is just starting to appear a few meters farther to the east, but it is not yet exposed well enough to be confident of its morphology. The trough between the two well-exposed lithic breccias is 33 m wide and 1.7 m deep and is filled with mLT (fig. 12A).

The convex lenses are interpreted as levees, with the flow direction into (and slightly oblique to) the outcrop. The nature of the flat contact between Units III and IV and the lack of obvious topographic influence upstream from this location further suggests that the levee depositional features at this location are a consequence of flow self-channelization where the nonuniformity of a flow spreading across a low-sloping fan develops zones of faster moving flow axes known as thalwegs (for example, Imran and others, 1998; Branney and Kokelaar, 2002). Levees can form as the result of (1) buildup of coarse material along the sides of a thalweg as deposition occurs in lateral static zones along channel margins (Félix and Thomas, 2004) and (or) (2) increased friction along the outside of the flow behind the flow head and rotation of the velocity vector from the downslope direction along the center of the thalweg to the transverse direction toward the channel margins (Mangeney and others, 2007).

Regardless of the mechanism of formation, the lithic levees suggest self-channelization within the PDC that produced Unit IV. We interpret that each strata within the levees represents a different time surface as the current flowed and the deposit aggraded, which suggests deposition from a sustained but locally unsteady current. The thick, block-poor mLT fill between the levees and the thin mLT overlapping the levees suggests that these lithofacies were deposited during the waning phase of the Unit IV PDC. The thinning of mLT over the levees is evidence that the later flow overtopped the levees and that the surface roughness and levee features affected and partially channelized the waning phases of the current.

## Stop 6: Outcrop D-4

Outcrop D-4 is 0.24 km northwest of outcrop C-4 (fig. 6). The outcrop is ~5.5 km from the source. Two convex breccia lenses at the base of Unit IV (figs. 12*B,* 12*C*, and 13) closely resemble those found at outcrop C-4. The similarity in morphology suggests they represent a downstream cross section through the same levee system.

The western convex lens is ~55 m in wavelength and is composed of lithic breccia with crude fabric. The eastern levee is 82 m in wavelength, although several smaller, convex, imbricated lenses within the eastern portion may explain the longer wavelength relative to the western levee. The two main convex lithic breccias are separated by a 45-m-wide trough of mLT. Measurements taken from the center of the trough at both outcrops C-4 and D-4 indicate a flow direction of N. 30° W., which coincides with the mapped flow direction on the Kuntz and others (1990) map. The P-value of the eastern levee is 0.03, which is below but still near the confidence interval of 0.05. This observation suggests that, while some substrate entrainment likely occurred as the flows passed through the breach, there was not significant enough erosion to cause exceptionally low P-values. Therefore, we interpret that the levees developed independently

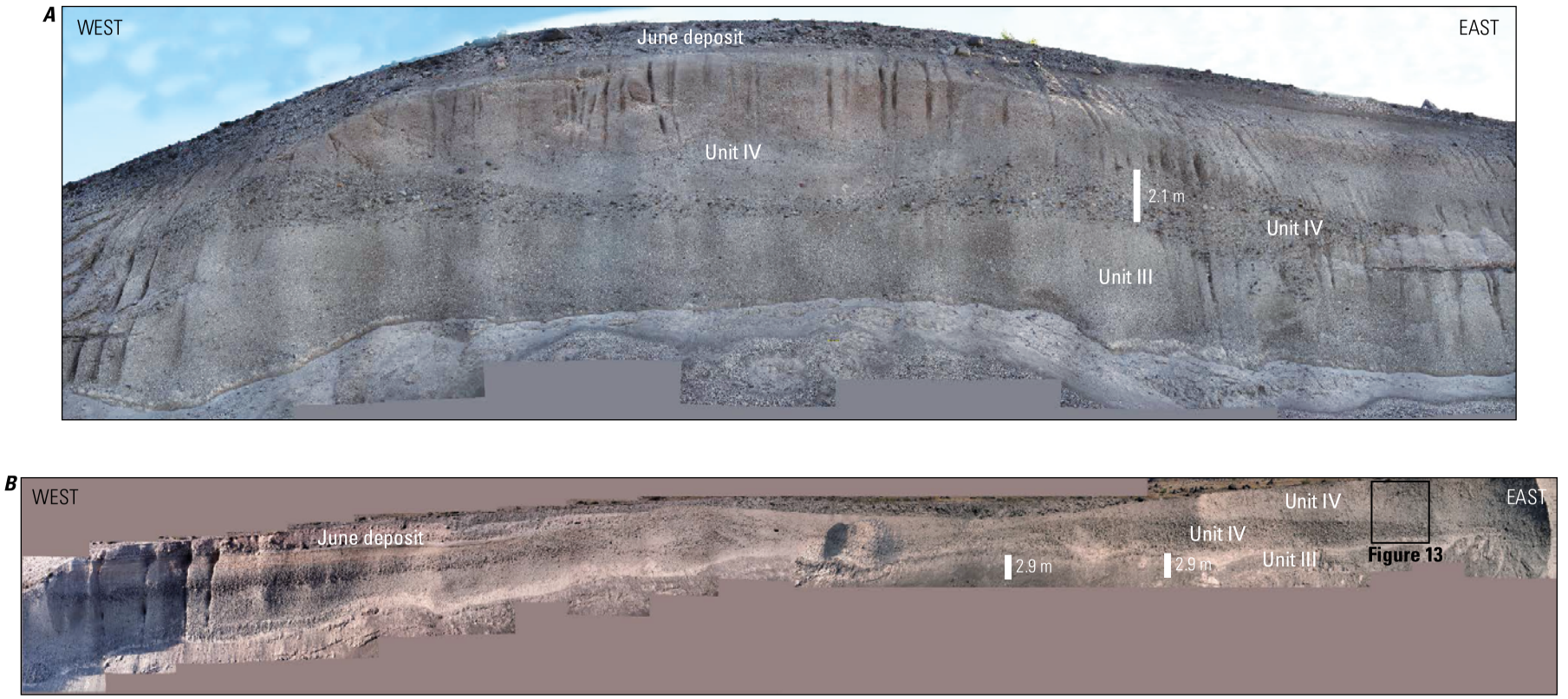


**Figure 12.** *A*, High-resolution composite photograph of outcrop C-4 (Stop 5; see fig. 6 for location), with the two convex block-rich breccias of Unit IV deposits interpreted to be levees. *B*, High-resolution composite photograph of outcrop D-4 (Stop 6). Similar convex block-rich breccias are interpreted to be the larger, downstream continuation of the levees seen in outcrop C-4 (Unit IV). Using the midpoints of the two channels, the flow direction ranges N. 25–30° W. (roughly), oblique but into both outcrops C-4 and D-4.

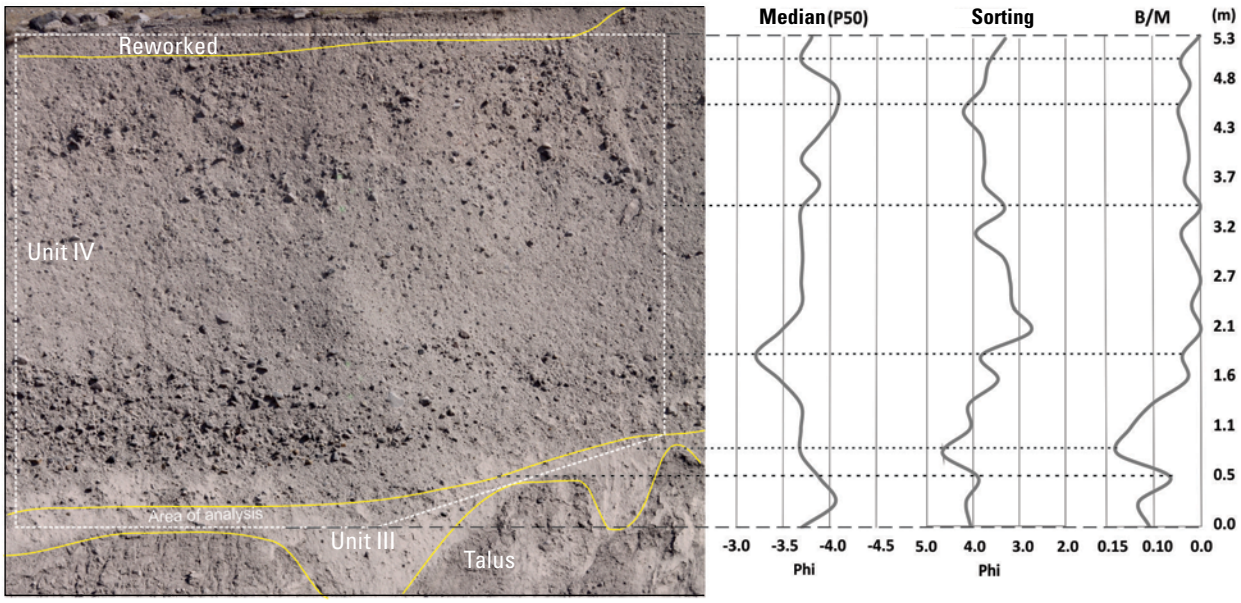


**Figure 13.** Vertical granulometric profiles of median (P50), sorting, and block-to-matrix (B/M) ratio for enlarged area delineated in figure 12*B*. LROG data illustrates the granulometric differences and the change of granulometric trends between the different units.

of interaction (for example erosion) with complex topography (Pollock and others, 2016).

## Stop 7: AD-1

Outcrop AD-1, the first outcrop past the C-D drainage convergence (fig. 6), is located ~0.12 km west-southwest from outcrop D-4. The dominant flow direction is parallel or slightly oblique to the outcrop shown in figure 7. Unit I is exposed at the base of outcrop AD-1, which is located 5.7 km from the source. It is present as fines-depleted dxsLT capped with a thin (<50 cm) layer of fine-grained, massive ash (fig. 7). It is 2.6 m thick at this location, although the base is not exposed. Unit I has a sharp contact with Unit II. Unit II is characterized as 2.2- to 3.6-m-thick, fines-depleted, reverse-graded dsLT. Coarse-grained, poorly sorted lensP is common in both units. Unit II is locally capped by a 20- to 50-cm-thick layer of fine-grained, massive ash (fig. 7*C*).

The stratified nature and fines-depleted deposits of Units I and II suggest conditions in the depositional region of the PDCs ranged from a semi-fluidized, granular flow boundary to a traction-transport, flow-boundary zone (Branney and Kokelaar, 2002). Basal shear stresses were high enough to form distinct, albeit poorly developed, stratification. Turbulence may have locally been an important particle transport mechanism in the current responsible for Unit I as evidenced by the diffuse cross-stratification at outcrop AD-1. The laterally continuous nature of the fines-enriched mT capping Units I and II suggests deposition from the waning tail of a PDC, a coignimbrite ash that settled after the PDC ceased, or some combination of the two processes (fig. 7*C*).

Unit III at outcrop AD-1 is the 5- to 7-m-thick, block-rich, poorly sorted $mLT_{bl\text{-}f}$. The first ~3 m of Unit III displays reverse grading of lithic blocks. The largest five lithic blocks range from 40 to 70 cm in their longest dimension. The blocks have weak fabric and appear to splay at 13–17° to the north (figs. 7 and 8). Meter-scale, convex lithic lenses (lenslBr) with strong fabric and stratification are common. The lithic lenses produce a discontinuous but wavy surface across the outcrop, which is capped by finer-grained mLT (fig. 7*B*, letters a, b, and c).

Unit IV is a massive, poorly sorted, variably lithic, block-rich unit that is 3.5–4 m thick. Reverse grading and fines-depletion are found within the lower 2.8 m, overlain by normal grading with an average amount of fines toward the top of the unit (figs. 7*A,* 7*B,* and 8). The five largest blocks range from 21 to 36 cm in their longest dimension; the average grain size of blocks is ~20–25 cm. However, unlike Unit III, the lithic blocks lack fabric and do not accumulate as lenslBr. Unit IV is capped by a thin veneer of the June 1980 PDC deposit (fig. 7).

The massive, poorly sorted, fines-normal nature of the deposit suggests rapid deposition from a PDC with a concentrated basal region. However, the block fabric in Unit III at outcrop AD-1, as illustrated with the thin dashed lines in figure 7*B*, suggests some influence of basal shear stress. Thus, the flow boundary for the PDC responsible for the deposition of Unit III at outcrop AD-1 is interpreted as a semi-fluidized, high-concentration flow.

Similar to Unit III, Unit IV at outcrop AD-1 was likely deposited by a concentrated current with rapid sedimentation and relatively low basal shear stress with minor fluctuations toward a granular flow boundary, as evidenced by the predominantly

massive nature and weak to nonexistent fabric. The normal grading suggests deposition from a waning current. The range from fines depleted to fines normal suggests that the process of elutriation, likely due to sedimentation fluidization, continued to occur this far from the source within the basal region of the current. This marks the farthest lateral extent of fines depletion found within Unit IV.

Many of the contacts between Units III and IV at outcrops AD-1 through AD-3 are indistinct or completely unrecognizable. In general, the diffuse or indistinct flow boundaries are interpreted to reflect variable erosion and shear-derived mixing with the earlier flow deposits (for example, Calder and others, 2000; Rowley and others, 2011). The most striking example of completely erased flow boundaries occurs where outcrop AD-1 transitions from the east side of the outcrop, where flow contacts are somewhat recognizable, to a thick wall of $mLT_{BI}$ on the west side of the outcrop, where evidence for flow boundaries between Units II, III, and IV are not apparent.

Note on the map in figure 4*E* that the currents depositing on the west side of outcrop AD-1 were likely traveling from southeast to northwest (from the breach), but parts of the currents were also following a flow path down the west flank. We interpret that the lack of distinct flow boundaries is due to increased frictional forces at the bed, because the upstream break in slope is from 10° to <5°, which affected the portions of the current traversing the west flank (figs. 5 and 6; Sulpizio and Dellino, 2008; Sulpizio and others, 2008). The break in slope likely caused shear-derived mixing, followed by rapid deposition from the basal region of the current, resulting in massive deposits that lack clear flow unit boundaries (Kneller and Branney, 1995; Giordano, 1998; Branney and Kokelaar, 2002; Pittari and others, 2006; Sulpizio and others, 2008). The lack of flow boundaries is important to consider when studying PDC deposits with limited exposure, because a section could easily be misinterpreted as the consequence of a single sustained current rather than multiple currents with amalgamated flow contacts.

## Stop 8: Outcrop AD-2a

- Hike 0.8 km downstream, staying inside the drainage, to outcrop AD-2a.

**Note**: Recent erosion between 2014 and 2015 exposed deposits from the lateral blast along the drainage on the way to AD-2a. Blast deposits are distinguished by the presence of prismatic-joined dacite blocks, which represent the crytodome material.

Outcrop AD-2a is located 5.63 km from the vent and north of a series of debris-avalanche hummocks (fig. 6). The south side of the outcrop exposes one of the debris-avalanche hummocks in contact with PDC deposits to the north (fig. 14). The contact between the debris avalanche and PDC deposit is sharp and has an apparent dip that varies from nearly vertical to 45°. PDCs deposited on the north side of the debris-avalanche hummock likely traveled around it from both sides, potentially colliding (see fig. 4*E* for flow-direction interpretations, based on Brand and others, 2014).

Outcrop AD-2a contains a variety of mLT and mlBr, including lenses and layers that vary both laterally and vertically. The lowermost portion of the outcrop is composed of a light-toned mLT (figs. 14*D* and 14*C*, region A), which has a fairly sharp contact with the overlying, slightly darker $mLT_{bl}$ (fig. 14*D* and 14*C*, region B; contact best exposed on north side of outcrop). Region B is in contact with the debris-avalanche hummock on the south side of the outcrop and contains a variety of lithic block concentrations that vary across the outcrop. Near the base of region B is a layer of semi-continuous, poorly developed lenslBr that varies in thickness from 0.1 to 3 m (figs. 14*D*, sample S4). Lithic blocks in the lenses are up to 0.7 m in diameter and have no obvious preferred orientation. Above lenslBr on the south and middle portions of the outcrop is a variable-thickness $mLT_{bl}$. To the north, the basal block-rich layer grades laterally into $mLT_{bl}$, where the lithics are more evenly dispersed (fig.14*D*, region B, sample S6).

Above the region B, mLT in the northernmost part of the outcrop is region C, a thick $mlBr_f$ that thins to the south and eventually disappears (figs. 14*A* and 14*B*, sample S7). The region B breccia is up to 5 m thick, normally graded, and displays weak fabric due to grain alignment toward the base, where the largest blocks are up to 0.6 m in diameter. The breccia is overlain by the region D block-poor mLT that varies in thickness from 0.1 to 3.5 m (figs. 14*A* and 14*B*). The mLT extends to the south where it pinches and swells before completely pinching out below the block-rich accumulation of region E.

In region E, $mlBr_f$ is ~5 m thick and 30 m long and continues across the small drainage that cuts up through the center portion of the outcrop (figs. 14*A* and 14*B*, sample S5). The block accumulation shows weak imbrication and thins and bends upwards to the north, where it overlies mLT of region D and lenslBr of region C. Lithics in the region E block-rich facies are up to 0.9 m in diameter. Below the southernmost portion of the region E lithic accumulation, the contact with the underlying mLT (region D) undulates; the overlying block-rich facies of region E appears to sink downward into the underlying mLT. The southern margin of the block-rich accumulation of region E is a steeply dipping contact with a relatively block-poor mLT (region F). This mLT extends to the south and overtops the debris avalanche hummock, eventually thinning and disappearing at the far southern extent of the outcrop.

The chaotic assemblages represented in outcrop AD-2a are likely the consequence of collision between PDCs that simultaneously traveled across the west flank and through the breach. The lack of flow-unit boundaries suggests shear-derived mixing was important at this location as well, likely due to higher shear at the base (indicated by the block fabric) and mixing between currents as they collided. Block accumulations (figs. 14*A* and 14*B*) have P-values that vary from very low (<0.001; samples S6, S7) to relatively high (0.17; sample S5), indicating a mixture of lithic blocks eroded from the vent and from upstream hummocks. The larger, vent-derived lithic block accumulations are interpreted as a consequence of the flows along the west flank maintaining a higher flow competence than those that traveled through the breach (due to fewer breaks in slope and a shorter,

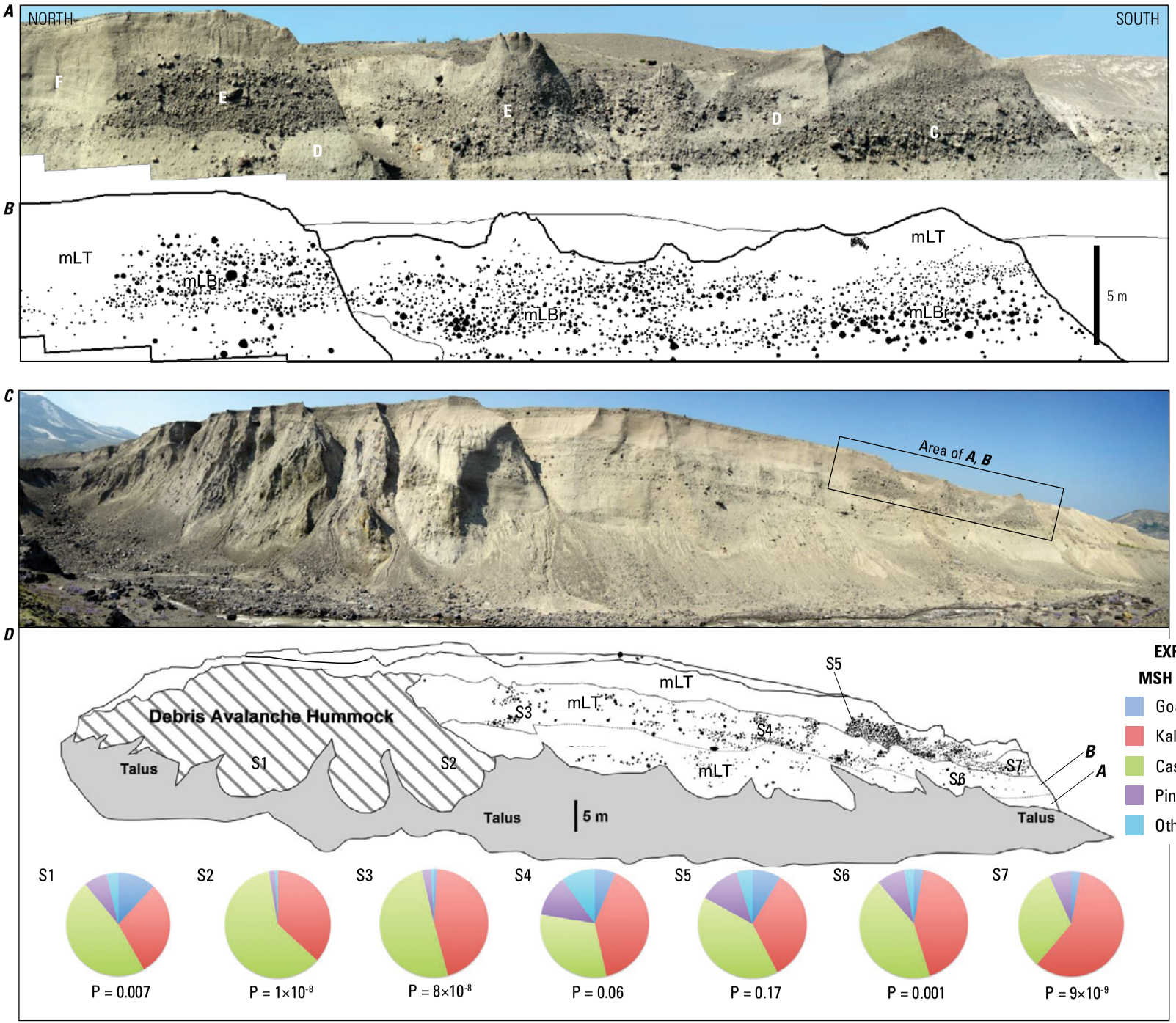


**Figure 14.** Details of outcrop AD-2a (Stop 8; see fig. 6 for location). Labels C–F represent different facies described in the text. Enlarged photograph (*A*) and labeled sketch (*B*) of area delineated in *C*. *C*, Photograph of outcrop AD-2a looking west. *D*, Sketch of photograph C showing units and features. Numbers (S1–S7) indicate sample locations and associated pie charts represent componentry.

unobstructed and relatively smooth flow path). Because we cannot determine the exact upstream source of the locally eroded lithic blocks, it is not possible to determine over what distances eroded material was carried before depositing at outcrop AD-2a. The undulating appearance at the base of many of the lithic breccias is likely a result of loading and deformation of the underlying deposits by mlBr above.

## Stop 9: Outcrop AD-3

- Hike 0.7 km downstream, staying inside the drainage, to outcrop AD-3.

Outcrop AD-3 is a 400-m-long outcrop oriented north-south, exposing Units I–IV (fig. 6). Flow direction was roughly into the outcrop from the southwest (figs. 4*D* and 4*E*). The contact between Units I and II is distinct and serves as a stratigraphic marker across the outcrop (figs. 15*A* and 15*B*). The contacts between Units II–III and III–IV are indistinct, suggesting erosion and amalgamation of later currents with earlier current deposits.

A notable feature in outcrop AD-3 is a small phreatic crater, located on the south side of the outcrop (fig. 15). The explosion crater is rimmed by a thin veneer of cross-stratified, base-surge deposits (type of dilute PDC), which were generated by the phreatic explosion and extend over a few tens of meters away from the rim. The crater is filled with a lahar deposit and capped with wind-blown ash. Two additional explosion craters are just beginning to be exposed on the north side of the outcrop. One is at the Unit I–II flow boundary contact, and the other is cropping out through Unit IV.

Note that Unit I in this location is 13 m thick, although the base is not exposed. It is also more massive than the stratified deposits found in Unit I at outcrop AD-1. The pumice lenses are coarser, thicker, and more abundant. Wave- or flame-like structures that extend toward the north are present just to the right of the explosion crater (fig. 16*A*) and are interpreted to represent shear-induced deformation at the depositional boundary and a flow direction of roughly south to north.

Unit II is 8 m thick but truncated by the Unit III flow-boundary contact on the north side of the outcrop, which is the beginning of a 200-m-wide, broad, scour-and-fill feature (figs. 15 and 16). The scour occurs at the contact between Units II and III, where the PDC responsible for Unit III was first erosional, scouring down through Unit II, then depositional, filling the scour with mLT and mlBr. The scour contains Units III and IV, which extend toward the north side of the outcrop and are oriented with a dip towards the center of the feature (fig. 17).

The first 2–3 m of Unit III (within the scour) is mLT, which transitions abruptly into 0.3- to 1.8-m-thick, lithic, block-rich mlBr, which extends 60 m along the south side of the scour toward the axis. The five largest blocks within the scour, which are composed solely of lithics, range from 69 to 100 cm in their longest dimension; the average grain size of blocks is ~82 cm (figs. 17 and 18). Blocks appear weakly oriented and their longest (apparent) axis is parallel to the bedding plane. The block-rich region abruptly grades into normally graded mLT with <2 percent blocks (figs. 15 and 17), which thins away from the center of the feature.

Unit IV overlies Unit III within the scour; a sharp and erosional contact is present between Unit IV and Unit III. Unit IV is up to 3.5 m thick; however, the top may not be fully preserved. The base of Unit IV is distinguished by a 0.62- to 2.25-m-thick concentrated zone of lithic blocks (mlBr). The average block size at the base of the massive breccia ranges from 0.20 to 0.40 m and fines upward to an average block size of 0.12–0.15 cm (figs. 17 and 18). The five largest blocks range from 70 to 95 cm in their longest dimension. Like the lithic breccia in unit III, the blocks, composed solely of lithics, are weakly oriented and their longest apparent axis is parallel to the bedding plane (fig. 17).

The block-rich region shows normal grading and a slight reverse grading at the top of the concentration towards the center of the scour and is overlain by mLT (fig. 17). The outer channel deposits to the south contain elongated lensP, and diffuse strata that dip 2–3° away from the axis of the channel (fig. 17) are interpreted to be the result of the upper portion of a density stratified current that overtopped the channel margins, depositing the less dense (lensP) and finer-grained material. The diffuse contact between Units III and IV outside of the channel is interpreted to be the result of amalgamation (for example, Calder and others, 2000; Rowley and others, 2011). Note also the presence of wave- or flame-like structures that extend toward the north, just outside the left margin of the channel (fig. 16*B*). This is interpreted as a shear-induced flame structure, similar to those described at outcrops C-3 and B-2a, and indicates a flow direction parallel to the outcrop. Thus, multiple flow directions are likely for this location as well (see flow lines in fig. 4*D*).

Outcrop AD-3 represents the medial-distal outlet of the currents that traveled through the breach and (or) along the northwest flank. The PDC responsible for Unit III carved a large, wide channel into the Unit II deposits. This is an example of self-channelization where the current spreading across the flat pumice plain developed zones of higher flow energy, causing the flow to preferentially channelize and erode into the underlying substrate. Within the channel, the deposits begin with mLT, suggesting the erosive current eventually became depositional and progressively filled the channel as the concentrated current continued to pass. The abrupt increase in vent-derived blocks (mlBr; see high P-values in fig. 17) with no obvious break in deposition suggests an increase in mass flux and lithic material at the vent (for example, Branney and Kokelaar, 2002). The outsized blocks relative to nearby Unit III and IV deposits suggest that channelization of Unit III allowed the current to transport larger blocks farther from the source. The sharp interface between mlBr and overlying mLT in both Units III and IV suggests a sharp density gradient between the large, dense blocks that segregated to the base of the flow and the overlying mixture of gas, ash, and lapilli (pumice, lithic). The fabric observed in mlBr, where the blocks are oriented with their longest apparent axis parallel to the bedding plane, suggests granular flow-boundary conditions; whereas, the lack of fabric, poor sorting, and fines-normal nature of mLT suggests deposition from a concentrated basal region of

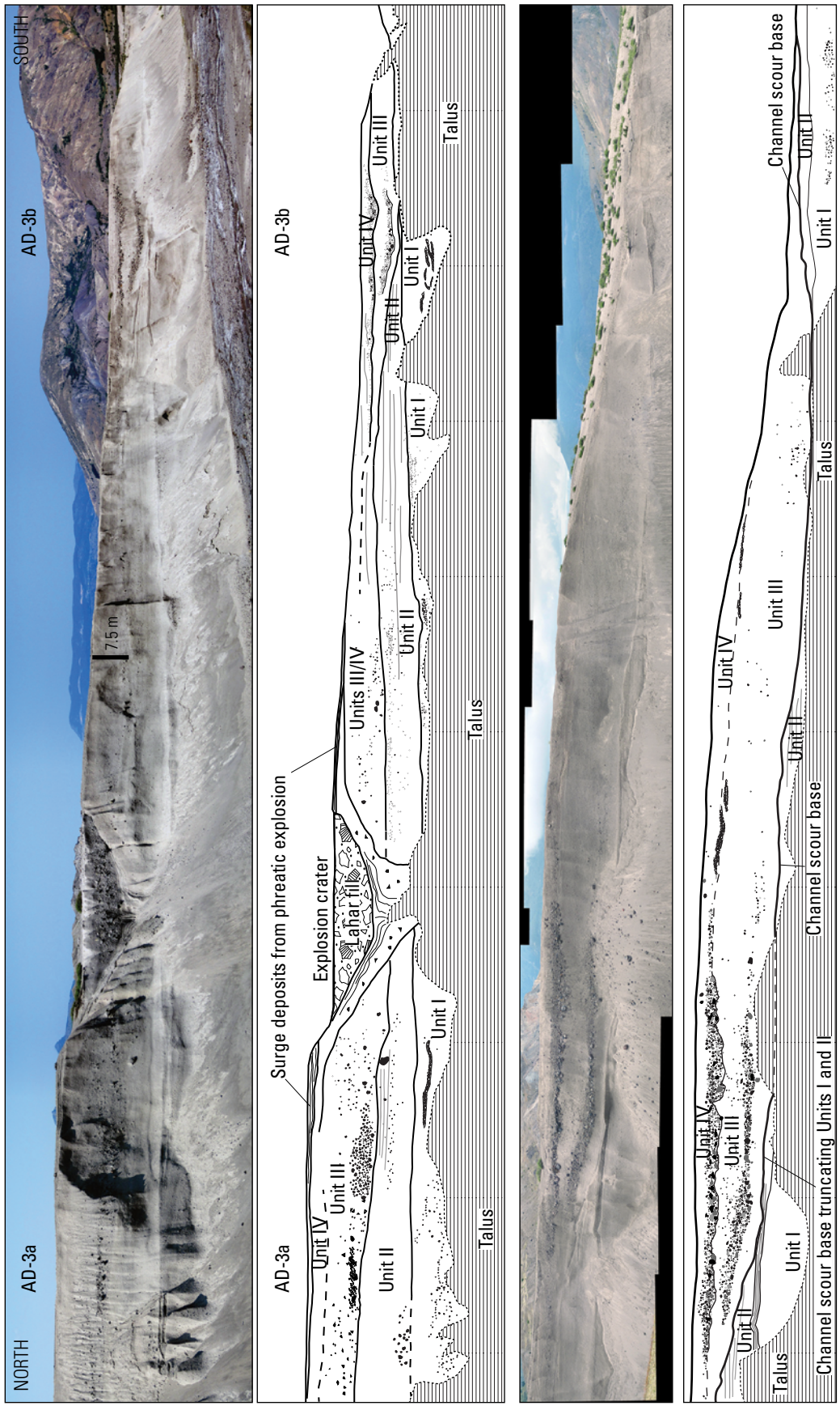


**Figure 15.** *A*, Photograph of outcrop AD-3 (Stop 9; see fig. 6 for location). *B*, Sketch of outcrop AD-3 showing outlined and labeled lithofacies and features. *C*, Photograph of outcrop AD-3b (north side of outcrop). *D*, Sketch of outcrop AD-3b showing outlined and labeled lithofacies and features.

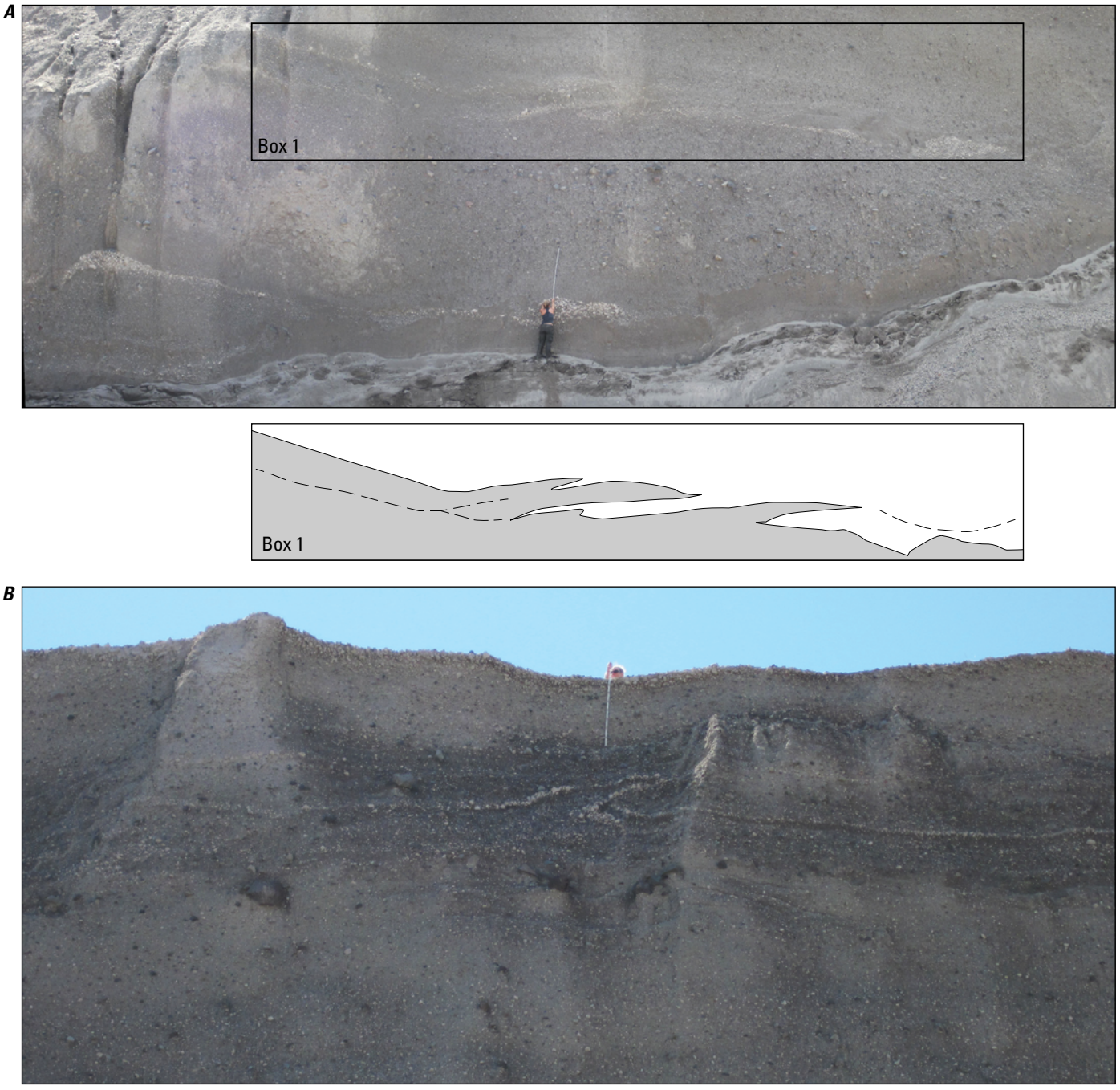


**Figure 16.** *A*, Photograph of Unit I exposed at outcrop AD-3 (see fig. 6 for location). Note weak, shear-induced flame structures in Box 1, trending south (right) to north (left), and associated sketch. *B*, Photograph of shear-induced flame structure trending south (right) to north (left), exposed in Unit IV at outcrop AD-3. Measuring stick is 1.8 m tall.

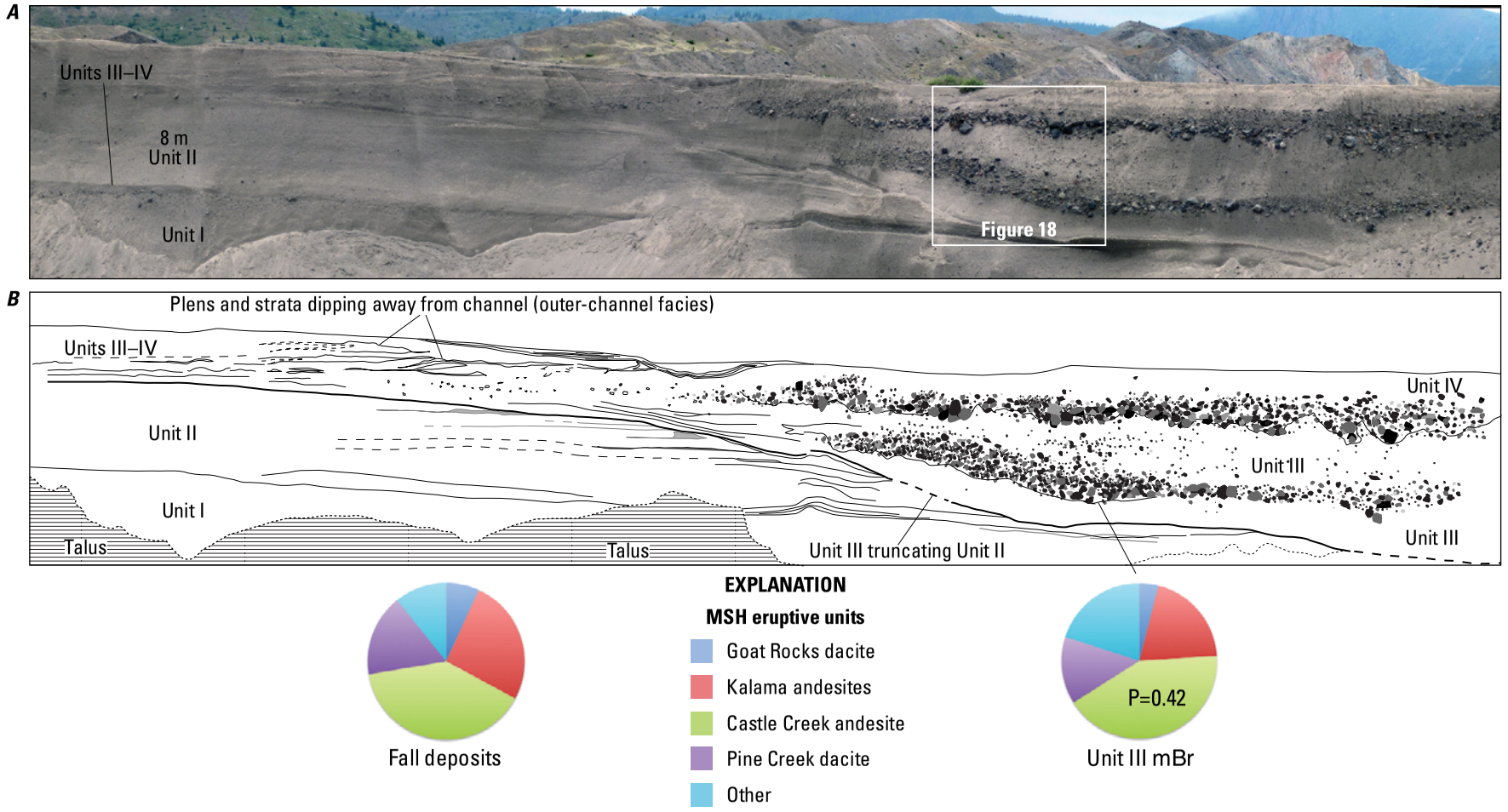


**Figure 17.** *A*, Photograph of northern-most outcrop AD-3 exposure (Stop 9; see fig. 6 for location). *B*, Sketch of outcrop AD-3 showing outlined and labeled lithofacies and features. Notice the truncation of Unit II by the channel-scour contact of Unit III. Also notice the outward-dipping strata and pumice lenses just to the left (south) of the channel, interpreted as outer-channel facies. Pie charts represent componentry of the block-rich, channel fill facies. Similarity of the fall deposits suggests the majority of lithics in channel fill were eroded from the vent (and not locally entrained).

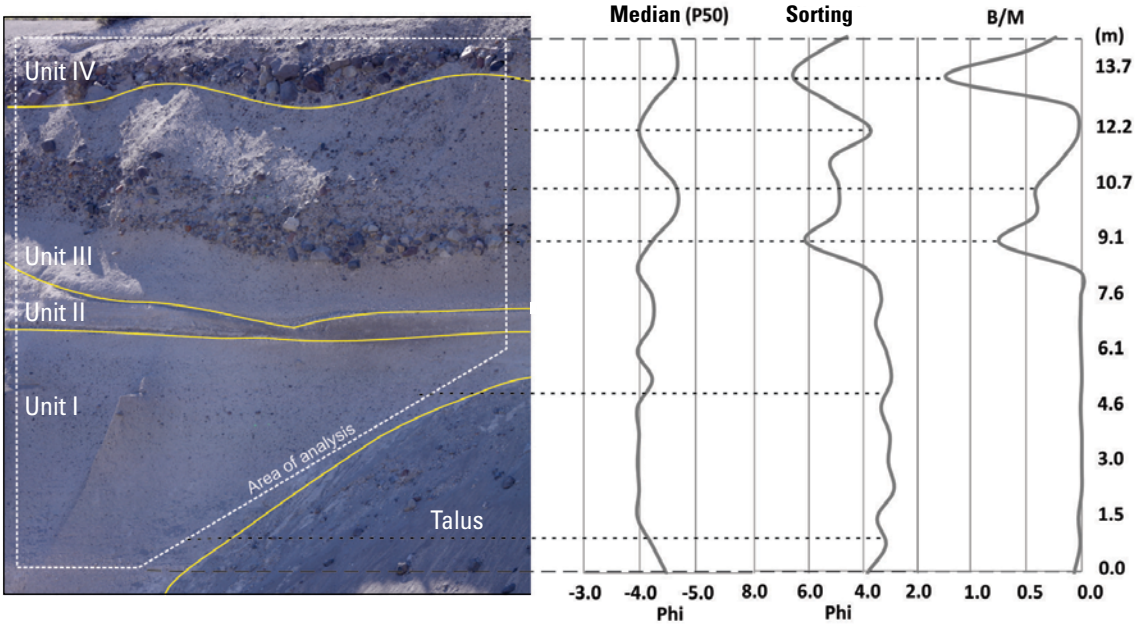


**Figure 18.** Vertical granulometric profiles of enlarged area, delineated in figure 17, showing median (P50), sorting, and block-to-matrix (B/M) ratio of areas shown in photograph. LROG data shows the presence of coarse symmetric (normal to reverse) gradations within Unit III.

the current with rapid sedimentation and lower basal shear stress relative to conditions that deposited the breccias.

## Stop 9 to Trailhead

- Hike 3.5 km east until you intersect Trail 207 (fig. 6). Due to the biology plots scattered across the pumice plain, the group must either stay within elk tracks or within drainages until reaching the trail.
- Follow Trail 207 for 3.2 km south, staying left at the one split in the trail, to the base of Windy Ridge (trailhead at base of parking lot).

# Day 4, Mount St. Helens Institute Field Camp to Trailhead (Driving); Trailhead to Loowit Falls and Stops 10 and 11 (Hiking)

### Mount St. Helens Institute Field Camp to Trailhead

- From Cascade Peaks parking lot, turn left on NF–99 and drive 5.6 mi to the Windy Ridge Viewpoint parking lot (fig. 1). We will pass through the (locked) gate on the south side of the parking lot.
- After passing through the gate, we will drive 2.0 mi down a gravel path to the main trailhead at the base of the ridge (gravel road is marked as Trail 207 on the National Forest Service trail maps).

### Trailhead to Loowit Falls

- Take Trail 216 from the junction just past the parking lot.
- Hike 1.3 km to split in trail, then continue west (right) on Trail 216E.
- Hike 2.25 km to Loowit Falls, Stop 10.

### Loowit Falls to Flank Deposits

- From Loowit Falls, return along Trail 216E for 0.8 km to (UTM 563858 E., UTM 5119720 N.).
- Turn south (right) and hike directly upslope for 0.4 km to Stop 11 (UTM 563668 E., UTM 5119331 N.).
- Continue 0.6 km upslope to Stop 10 (UTM 563369 E., UTM 5118802 N.).
- Return to Trail 216E by hiking downslope to north.
- Hike Trail 216E back to trailhead, staying right at the fork.

## Stop 10: Proximal Bedded Deposits (PBD)

For bedforms in the proximal bedded deposits (along steep flanks), form height refers to the thickest part of the bedform crest (often referred to as wave height). Wavelength is the distance between successive crests; form length is the horizontal distance between the first stoss side to the last lee side expression. Form length was also recorded, because consecutive bedforms were not always exposed to measure wavelength.

The following description comes from Brand and others (2016). The upper flank PBD deposits are primarily composed of stratified and cross-stratified deposits that create large-scale dune bedforms and small-scale, subsidiary dune bedforms. Regressive dune bedforms, which are low-angle, broad bedforms with thick, well-developed strata on the stoss side and generally thinner strata on the lee side (figs. 19*A* and 19*B*), are found on depositional slopes of 10–28°. Isolated bedforms have form lengths from 2 to 15 m and form heights from 0.5 to 5 m. Where found, consecutive bedforms had wavelengths from 2 to 8 m (no longer exposed). Cores of regressive dune bedforms with steeply dipping backset bedforms are truncated on the stoss side by steeply upflow-dipping truncation surfaces (from 30° up to an extreme of 68°) with a sigmoidal shape. A series of well-developed, thick, upflow-stacking beds, also sigmoidal in shape, are found upstream and have accumulation lengths up to 15 m (figs. 19*A* and 19*B*). These steeply dipping backset beds are only found on slopes of 15–26°.

Progressive dune bedforms, low-angle, broad bedforms with thick, well-developed strata on the lee side, are found on depositional slopes of 12–16°. Isolated bedforms have form lengths from 2 to 14 m and form heights from 0.4 to 2.5 m. Where found, consecutive progressive bedforms have wavelengths from 3 to 7.6 m.

We interpret that portions of the concentrated afternoon PDCs were funneled between Sugar Bowl dome and a topographic high to the east then accelerated and thinned as they descended and spread across the steep slope (Brand and others, 2016). The concentrated basal region of the current(s) thinned until the overriding turbulence strongly influenced transport and deposition, and the basal region behaved as a bedload at the base of a dominantly supercritical, turbulent flow that marked a major change in current dynamics.

The high surface roughness along the flanks suggests that mechanisms for autofluidization described by Chédeville and Roche (2014, 2015), where an upward air flux results from substrate interstices as flow particles settle between grains, may have been important for the May 18, 1980, PDCs descending the steep flanks. The experiments of Bareschino and others (2008) demonstrate that increased velocities resulted in flow-front instabilities and "plunging breakers," where the upper portion of the current head extends beyond the basal region (overhanging) and collapses as an avalanche, resulting in substantial entrainment of ambient air. Given evidence for thinning of the current and interaction with irregular topography along the east flanks, plunging breakers could be another source of air entrainment.

Evidence for supercritical flow conditions (high flow-regime bedforms) also suggests that entrainment of ambient air would be important along the steep flanks, further influencing flow dynamics (Bursik and Woods, 1996). Flow criticality is governed by the ratio of the inertia forces over gravitational forces, which is represented by the Froude numbers (Fr),

$$\mathrm{Fr}=Ug'h, \tag{1}$$

where

$$\mathrm{Fr} = \frac{U}{\sqrt{g'h}} \tag{2}$$

$U$ is velocity and
$h$ is the flow depth.

Reduced gravity is accounted for using the following equation:

$$g' = g\left(\frac{(\beta-\alpha)}{\alpha}\right) \tag{3}$$

where

$g$ is the gravitational acceleration,
$\beta$ is the bulk density of the current, and
$\alpha$ is the density of the atmosphere.

Studies in open channel flow show that progressive bedforms develop under subcritical conditions where Fr <1, and regressive bedforms develop under supercritical conditions where Fr >1 (Blatt and others, 1980). Thus, in addition to simple thinning of the basal region of the current, expansion of the currents due to autofluidization and ambient air entrainment also likely served to change flow behavior from that of concentrated PDC conditions to relatively dilute, turbulent PDC conditions, as described above.

The generally fines-normal PBD suggest that comminution of pumice and the addition of fine ash kept up with elutriation. Comminution is further supported by the subangular to subrounded nature of the pumice, which suggests that pumice clasts were in a state of active but incomplete rounding upon deposition along the steep flanks. Comminution can result in a significant increase in the fines proportion (Dufek and Manga, 2008; Manga and others, 2011; and references therein) and is the most likely explanation for the fines-normal nature of the PBD.

Componentry was measured following the methods of Pollock and others (2016) in two locations at Stop 11 (figs. 19*D* and 19*E*). Both samples are enriched in Castle Creek andesite, which is exposed in the canyon directly upstream, and have P-values <<0.05, providing statistical evidence for upstream substrate erosion in both bed sets. These findings are consistent with the results of Bernard and others (2014) and Calder and others (2000), who find that substrate erosion is promoted at slopes of ~25° (former) and in the presence of topographic obstacles or constrictions (latter).

The largest blocks of andesite of Castle Creek found in each sample range from 8 to 29 cm in their longest direction. The theoretical approach of Roche (2015) demonstrates that, for a dilute, turbulent PDC traveling across a 10° slope, the largest dense lithic that can be entrained is 18 cm (for densities of 2,000–3,000 kg/m$^3$). However, the simplifying assumptions in Roche (2015) break down for the PBD, because the surface roughness is significant (greater than a single clast diameter) and the current is not fully dilute. Regardless, the larger entrained blocks found along the flanks of Mount St. Helens suggest that dilute PDCs with concentrated basal regions are capable of entraining dense lithics up to 29 cm on slopes >25°.

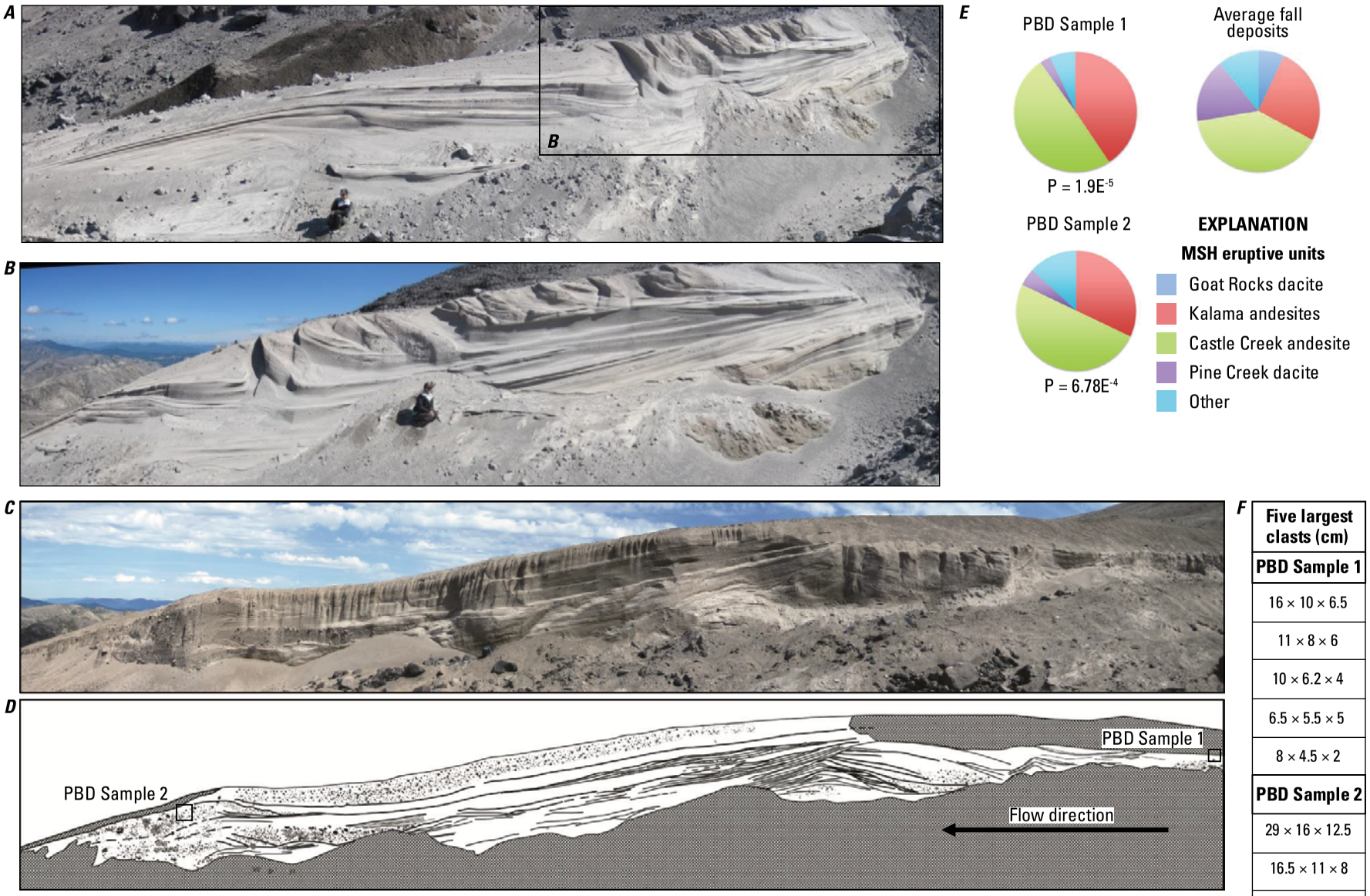


F

| Five largest clasts (cm) |
|---|
| **PBD Sample 1** |
| 16 × 10 × 6.5 |
| 11 × 8 × 6 |
| 10 × 6.2 × 4 |
| 6.5 × 5.5 × 5 |
| 8 × 4.5 × 2 |
| **PBD Sample 2** |
| 29 × 16 × 12.5 |
| 16.5 × 11 × 8 |
| 16 × 9 × 7 |
| 13 × 9 × 8 |
| 11 × 11 × 6 |

**Figure 19.** Photographs of the proximal bedded deposits, exposed along the east flank of Mount St. Helens. *A*, Photograph showing regressive bedform with prominent stoss-side accretion and a series of steeply dipping backset beds (flow direction right to left). *B*, Photograph of enlarged area showing backset beds. *C*, Photograph of deposits on middle to upper flank. Flow direction is from right to left. *D*, Sketch of outcrop outlining bedding features and blocks, flow direction, and sample locations. *E*, Pie charts comparing lithic componentry and P-values of pyroclastic-density-current (PDC) deposits to average fall deposits. *F*, Measurements of five largest lithic clasts of samples shown in D.

### Stop 11: Transitional Deposits

The PBD grade laterally (downslope) into less-stratified, massive deposits along the middle to lower flanks of the volcano (transitional facies; figs. 6 and 19*D*), ultimately grading into the main facies deposits of the eastern pumice plain (fig. 5*E*). This pattern likely reflects that, as flow energy decreases with distance and decreasing slope, the sediment supply from the upper portions of the current would increase, resulting in a thickening of the concentrated basal underflow. Thickening of the concentrated basal region due to increased sedimentation from the suspended load would suppress or eliminate the influence of turbulence from the overriding current. If the current has a high proportion of fines, as was the case for the May 18, 1980, PDCs, the basal region of the current may transition to a fluidized PDC with high internal pore pressure (for example, Roche and others, 2010). In addition, the ratio of the resisting stress to driving stress will increase as the slope decreases. Thickening of the underflow region and a decrease in slope would also result in a partial redirection of momentum flux per unit area (Iverson and Denlinger, 2001), effectively decreasing basal shear stress and increasing normal-bed frictional forces at the flow-deposit contact (Sulpizio and Dellino, 2008; Sulpizio and others, 2008). These conditions would promote deposition and offer an additional explanation for the thickening of deposits and lack of bedding features along shallow slopes.

## Discussion Points

As pyroclastic density currents with abundant fines compact during flow, permeability within the current reduces to such a degree that high internal pore pressure is sustained, allowing the currents to behave as highly mobile, fluid-like flows (for example, Roche, 2012). To what extent must the pore pressure diffuse to initiate deposition? Do fluidized currents with high internal pore pressure transition to granular flows where the influence of interstitial fluid is negligible, or can they deposit while the interstitial fluid is still present to buffer particle-particle interaction?

The first point of discussion is the role of fluidization and high internal pore pressure in PDCs with a high percentage of fines. The following evidence suggests that the May 18, 1980, afternoon PDC deposits at Mount St. Helens retained gas within the pore space, even after deposition:

- Soft-sediment deformation, caused by loading of lithic blocks over finer-grained deposits (for example, figs. 11*A* and 14*A*), is interpreted to represent the fluid-like and easily deformable nature of the deposits.
- A high proportion of fines, interpreted to suggest that elutriation became negligible in the basal portion of the current due to compaction during transport, would result in lower rates of pore-pressure diffusion.
- A lack of distinct, well-developed grain fabric (typical of granular flow), even in the distal regions, is interpreted to suggest that, while intergranular friction may have increased just before deposition, the interstitial gas remained to buffer interactions, preventing the flow from passing to a granular flow regime where the role of interstitial fluid was negligible.
- Numerous secondary breakaway PDCs occurred after the currents came to rest. Secondary PDCs occurred on slopes of 5–6° (Kuntz and others, 1990) and are interpreted to reflect relatively high pore pressure conditions within the PDC deposits.

A second point of discussion relates to the many elongated wave-like structures interpreted to represent shear-induced deformation and mixing of active currents with earlier PDC deposits as the currents aggraded (figs. 10*A*, 10*B*, 11*C,* and 16). These features, only exposed in the summer of 2016 due to recent outcrop erosion, suggest shearing was an active process at the flow boundary during aggradation of the deposits. What can we extract from these features that informs the nature of the current at the flow boundary just prior to and during deposition?

### Additional Discussion Points

- What are the processes (transport, erosional, and depositional) that govern PDC dynamics and ultimately affect runout and damage potential?
- What aspects of the total PDC are recorded by the deposits?
- How can we use the nature of substrate deformation and entrainment to investigate physical processes in or characteristics of the lower flow-boundary zone?
- Channelization of flows implies variable rates of deposition and erosion in a transient current. What are the dominant modes of erosion in PDC and local conditions that may favor one mechanism over another?
- How can we use eruptive deposits to constrain conditions that promote erosion by PDCs? Beyond the field, how can laboratory experiments and numerical modeling be combined with field observations to explore the causes and consequences of substrate erosion?
- There are many scales of transient flow in explosive eruption. To what degree do the eruptive deposits record variability at the source (for example, eruptive flux), interaction with large-scale topography, and evolving conditions in the flow-boundary zone?
- How much of the grain-size distribution recorded in the final deposit was modified from initial fragmentation during transport?
- What does the transport of large lithic clasts imply for momentum transfer mechanisms in PDC?
- Does self-channelization of flow promote longer runout distances in PDC or otherwise change mobility?
- What are the forces required to move the large lithic clasts observed in the field? What portion of the flow provides the energy for this transport?

# Itinerary

## Day 1: August 10, 2017

7–8:30 am: Breakfast at the Comfort Inn & Suites Portland, Portland, Oregon
9 am: Depart the Comfort Inn & Suites, Portland, for Mount St. Helens (fig. 1)
10 am: Grocery stop
11 pm: **Stratigraphy Viewpoint Pre-Pumice Plain Field Stop** and lunch
2–4 pm: Ape Caves hike
4 pm: Depart for Mount St. Helens Institute (MSHI) Field Camp at Cascade Peaks turnout (within the Mount St. Helens National Monument (figs. 1 and 2).
6 pm: Arrive at MSHI Field Camp. Shared tents, cots, and sleeping pads will be provided. Dinner will also be provided. However, participants must bring their own sleeping bag and other camping necessities (pillow, toiletries, extra clothing for the abrupt temperature drop at night).

## Day 2: August 11, 2017

6:30–7:30 am: Breakfast and packed lunches (provided)
7:30 am: Depart from MSHI Field Camp and drive to Windy Ridge
7:45–8:15 am: **Windy Ridge Viewpoint** and bathroom stop
8:15 am: Drive to pumice plain and begin ~1.5 hour hike
10:30 am–5 pm: Outcrop discussions at **Stops 1–4** (fig. 6)
5–6:30 pm: Hike to vehicles
7 pm: Return to MSHI Field Camp for dinner and overnight

## Day 3: August 12, 2017

6:30–7:30 am: Breakfast and packed lunches (provided)
7:30 am: Depart from MSHI Field Camp and drive to Windy Ridge
7:45–8 am: Bathroom stop at Windy Ridge
8 am: Drive to pumice plain and begin ~1.5 hour hike
9:30 am–5 pm: Outcrop discussions at **Stops 5–9** (fig. 6)
5–6:30 pm: Hike to vehicles
7 pm: Return to MSHI Field Camp for dinner and overnight

## Day 4: August 13, 2017

6:30–7:30 am: Breakfast and packed lunches (provided)
7:30–8:30 am: Break camp and pack vehicles
8:30 am: Depart from MSHI Field Camp and drive to Windy Ridge
8:45–9 am: Bathroom stop at Windy Ridge
9 am: Drive to pumice plain and begin ~1 hour hike to Loowit Falls Viewpoint (fig. 6)
10:30 am: Hike from Loowit Falls into crater (east side) to see flank deposits, **Stops 10 and 11** (fig. 6)
3 pm: Hike to vehicles
6:30 pm: Return to the Hilton Portland & Executive Tower, Portland, Oregon (fig. 1)

## References Cited


Andrews, B.J., and Gardner, J.E., 2009, Turbulent dynamics of the 18 May 1980 Mount St. Helens eruption column: Geology, v. 37, no. 10, p. 895–898.

Bareschino, P., Lirer, L., Marzocchella, A., Petrosino, P., and Salatino, P., 2008, Self-fluidization of subaerial rapid granular flows: Powder Technology, v. 182, no. 3, p. 323–333.

Bernard, J., Kelfoun, K., Le Pennec, J.L., and Vallejo Vargas, S., 2014, Pyroclastic flow erosion and bulking processes—comparing field-based vs. modeling results at Tungurahua volcano, Ecuador: Bulletin of Volcanology, v. 76, p. 1–16, doi: 10.1007/s00445-014-0858-y.

Blatt, Harvey, Middleton, G.V., and Murray, R.C., 1980, Origin of sedimentary rocks: Upper Saddle River, New Jersey, Prentice Hall, Inc., p. 782.

Brand, B.D., Bendaña, S., Self, S., and Pollock, N., 2016, Topographic controls on pyroclastic density current dynamics; Insight from 18 May 1980 deposits at Mount St. Helens, Washington (USA): Journal of Volcanology and Geothermal Research, v. 321, p. 1–17, http://dx.doi.org/10.1016/j.jvolgeores.2016.04.018.

Brand, B.D., Mackaman-Lofland, C., Pollock, N.M., Bendaña, S., Dawson, B., and Wichgers, P., 2014, Dynamics of pyroclastic density currents—Conditions that promote substrate erosion and self-channelization—Mount St. Helens, Washington (USA): Journal of Volcanology and Geothermal Research, v. 276, p. 189–214.

Branney, M., and Kokelaar, B.P., 2002, Sedimentation of ignimbrites from pyroclastic density currents: Memoir of the Geological Society of London, v. 27, p. 150.

Bursik, M.I., and Woods, A.W., 1996, The dynamics and thermodynamics of large ash flows: Bulletin of Volcanology, v. 58, p. 175–193.

Calder, E.S., Sparks, R.S.J., and Gardeweg, M.C., 2000, Erosion, transport, and segregation of pumice and lithic clasts in pyroclastic flows inferred from ignimbrite at Lascar Volcano, Chile: Journal of Volcanology and Geothermal Research, v. 104, no. 1, p. 201–235.

Carey, S., Sigurdsson, H., Gardner, J.E., and Criswell, W., 1990, Variations in column height and magma discharge during the May 18, 1980, eruption of Mount St. Helens: Journal of Volcanology and Geothermal Research, v. 43, p. 99–112.

Chédeville, C., and Roche, O., 2014, Autofluidization of pyroclastic flows propagating on rough substrates as shown by laboratory experiments: Journal of Geophysical Research, Solid Earth, v. 119, no. 3, p. 1764–1776.

Chédeville, C., and Roche, O., 2015, Influence of slope angle on pore pressure generation and kinematics of pyroclastic flows; insights from laboratory experiments: Bulletin of Volcanology, v. 77, no. 11, p. 1–13.

Christiansen, R.L., and Peterson, D.W., 1981, Chronology of the 1980 eruptive activity: U.S. Geological Survey Professional Paper 1250, p. 17–30.

Claiborne, L.L., Miller, C.F., Flanagan, D.M., Clynne, M.A., and Wooden, J.L., 2010, Zircon reveals protracted magma storage and recycling beneath Mount St. Helens: Geology, v. 38, p. 1011–1014, doi:10.1130/G31285.1.

Clynne, M.A., 2003, Mount St. Helens, South Flank Field Trip Guide: State of the Arc Conference, Timberline Lodge, Mount Hood, Oregon, August 16–21, 2003, 29 p.

Clynne, M.A., Calvert, A.T., Wolfe, E.W., Evarts, R.C., Fleck, R.J., and Lanphere, M.A., 2008, The Pleistocene eruptive history of Mount St. Helens, Washington—From 300,000 to 12,800 years ago, chap. 28 *of* Sherrod, D.R., Scott, W.E., and Stauffer, P.H., eds., A volcano rekindled—The renewed eruption of Mount St. Helens, 2004–2006: U.S. Geological Survey Professional Paper 1750, p. 593–627.

Clynne, M.A., Ramsey, D.W., and Wolfe, E.W., 2005, Pre-1980 eruptive history of Mount St. Helens, Washington: U.S. Geological Survey Fact Sheet 2005–3045, 4 p.

Crandell, D.R., 1987, Deposits of Pre-1980 pyroclastic flows and lahars from Mount St. Helens volcano, Washington: U.S. Geological Survey Professional Paper 1444, 91 p.

Criswell, C.W., 1987, Chronology and pyroclastic stratigraphy of the May 18, 1980, eruption of Mount St. Helens, Washington: Journal of Geophysical Research, Solid Earth (1978–2012), v. 92, no. B10, p. 10237–10266.

Doukas, M.P., 1990, Road guide to volcanic deposits of Mount St. Helens and vicinity, Washington: U.S. Geological Survey Bulletin 1859, 53 p.

Druitt, T.H., 1995, Settling behaviour of concentrated, poorly sorted dispersions and some volcanological applications: Journal of Volcanology and Geothermal Research, v. 65, p. 27–39.

Druitt, T.H., Avard, G., Bruni, G., Lettieri, P., and Maez, F., 2007, Gas retention in fine-grained pyroclastic flow materials at high temperatures: Bulletin of Volcanology, v. 69, no. 8, p. 881–901, doi:10.1007/s00445-007-0116-7.

Dufek, J., and Manga, M., 2008, In situ production of ash in pyroclastic flows: Journal of Geophysical Research, Solid Earth (1978–2012), v. 113, no. B9, p. 1–7.

Eisenhart, C., 1935, A test for the significance of lithological variations: Journal of Sedimentary Petrology, v. 5, p. 137–145.

Félix, G., and Thomas, N., 2004, Relation between dry granular flow regimes and morphology of deposits; formation of levées in pyroclastic deposits: Earth and Planetary Science Letters, v. 221, no. 1, p. 197–213.

Fisher, R.V., 1990, Transport and deposition of a pyroclastic surge across an area of high relief—The 18 May 1980 eruption of Mount St. Helens, Washington: Geological Society of America Bulletin, v. 102, no. 8, p. 1038–1054.

Giordano, G., 1998, The effect of paleotopography on lithic distribution and facies associations of small volume ignimbrites—the WTT Cupa (Roccamonfina volcano, Italy): Journal of Volcanology and Geothermal Research, v. 87, no. 1, p. 255–273.

Hausback, B.P., 2000, Geologic map of the Sasquatch Steps area, north flank of Mount St. Helens, Washington: U.S. Geological Survey Geologic Investigations Series 2463, 1 map, http://pubs.usgs.gov/imap/2463.

Imran, J., Parker, G., and Katopodes, N., 1998, A numerical model of channel inception on submarine fans: Jounal of Geophysical Research, v. 103, p. 1219–1238.

Iverson, R.M., and Denlinger, R.P., 2001, Flow of variably fluidized granular masses across three-dimensional terrain—1. Coulomb mixture theory: Journal of Geophysical Research, v. 106, no. B1, p. 537–552.

Kieffer, S.W., 1981, Fluid dynamics of the May 18 blast at Mount St. Helens: U.S. Geological Survey Professional Paper 1250, p. 379–400.

Kneller, B.C., and Branney, M.J., 1995, Sustained high-density turbidity currents and the deposition of thick massive sands: Sedimentology, v. 42, no. 4, p. 607–616.

Kuntz, M.A., Rowley, P.D., and MacLeod, N.S., 1990, Geologic maps of pyroclastic-flow and related deposits of the 1980 eruptions of Mount St. Helens, Washington: U.S. Geological Survey Miscellaneous Investigations Series Map I–1950.

Layer, P.W., and Gardner, J.E., 2001, Excess argon in Mount St. Helens plagioclase as a recorder of magmatic processes: Geophysical Research Letters, v. 28, no. 22, p. 4279–4282.

Macías, J.L., Espíndola, J.M., Bursik, M., and Sheridan, M.F., 1998, Development of lithic breccias in the 1982 pyroclastic flow deposits of El Chichon volcano, Mexico: Journal of Volcanology and Geothermal Research, v. 83, no. 3, p. 173–196.

Manga, M., Patel, A., and Dufek, J., 2011, Rounding of pumice clasts during transport; field measurements and laboratory studies: Bulletin of Volcanology, v. 73, no. 3, p. 321–333.

Mangeney, A., Roche, O., Hungr, O., Mangold, N., Faccanoni, G., and Lucas, A., 2010, Erosion and mobility in granular collapse over sloping beds: Journal of Geophysical Research, Earth Surface (2003–2012), v. 115, no. F3.

Mangeney, A., Tsimring, L.S., Volfson, D., Aranson, I.S., and Bouchut, F., 2007, Avalanche mobility induced by the presence of an erodible bed and associated entrainment: Geophysical Research Letters, v. 34, no. 22.

Moreno-Chavez, G., Sarocchi, D., Arce-Santana, E., and Borselli, L., 2015, Optical granulometric analysis of sedimentary deposits by color segmentation-based software—OPTGRAN-CS: Computer & Geosciences, v. 85, p. 248–257, doi:10.1016/j.cageo.2015.09.007 (ISSN: 0098-3004).

Mullineaux, D.R., 1986, Summary of pre-1980 tephra-fall deposits erupted from Mount St. Helens, Washington State, USA: Bulletin of Volcanology, v. 48, p. 17–26.

Mullineaux, D.R., 1996, Pre-1980 tephra-fall deposits erupted from Mount St. Helens, Washington: U.S. Geological Survey Professional Paper 1563, 99 p.

Pittari, A., Cas, R.A.F., Edgar, C.J., Nichols, H.J., Wolff, J.A., and Marti, J., 2006, The influence of palaeotopography on facies architecture and pyroclastic flow processes of a lithic-rich ignimbrite in a high gradient setting—the Abrigo Ignimbrite, Tenerife, Canary Islands: Journal of Volcanology and Geothermal Research, v. 152, no. 3, p. 273–315.

Pollock, N., Brand., B.D., and Roche, O., 2016, The causes and consequences of substrate erosion in pyroclastic density currents: Journal of Volcanology and Geothermal Research, v. 325, p. 135–147.

Roche, O., 2012, Depositional processes and gas pore pressure in pyroclastic flows—an experimental perspective: Bulletin of Volcanology, v. 74, no. 8, p. 1807–1820.

Roche, O., 2015, Nature and velocity of pyroclastic density currents inferred from models of entrainment of substrate lithic clasts: Earth and Planetary Science Letters, v. 418, p. 115–125.

Roche, O., Montserrat, S., Niño, Y., and Tamburrino, A., 2010, Pore fluid pressure and internal kinematics of gravitational laboratory air-particle flows; insights into the emplacement dynamics of pyroclastic flows: Journal of Geophysical Research, v. 115, no. B09206, doi:10.1029/2009JB007133.

Rowley, P.D., Kuntz, M.A., and MacLeod, N.S., 1981, Pyroclastic-flow deposits: Geological Survey Professional Paper 1250, p. 489–524.

Rowley, P.D., MacLeod, N.S., Kuntz, M.A., and Kaplan, A.M., 1985, Proximal bedded deposits related to pyroclastic flows of May 18, 1980, Mount St. Helens, Washington: Geological Society of America Bulletin, v. 96, no. 11, p. 1373.

Rowley, P.J., Kokelaar, P., Menzies, M., and Waltham, D., 2011, Shear-derived mixing in dense granular flows: Journal of Sedimentary Research, v. 81, p. 874–884, doi:10.2110/jsr.2011.72.

Sarocchi, D., Borselli, L., and Macías, J.L., 2005, Construcción de perfiles granulométricos de depósitos piroclásticos por métodos ópticos: Revista Mexicana de Ciencias Geológicas, v. 23, no. 2, p. 371–382.

Sulpizio, R., and Dellino, P., 2008, Sedimentology, depositional mechanisms, and pulsating behaviour of pyroclastic density currents: Developments in Volcanology, v. 10, p. 57–96.

Sulpizio, R., De Rosa, R., and Donato, P., 2008, The influence of variable topography on the depositional behaviour of pyroclastic density currents; the examples of the Upper Pollara eruption (Salina Island, southern Italy): Journal of Volcanology and Geothermal Research, v. 175, no. 3, p. 367–385.

Yamaguchi, D.K., and Hoblitt, R.P., 1995, Tree-ring dating of pre-1980 volcanic flowage deposits at Mount St. Helens, Washington: Geological Society of America Bulletin, v. 107, no. 9, p. 1077–1093.

Menlo Park Publishing Service Center, California
Manuscript approved March 19, 2017
Edited by J.L. Zigler
Design and layout by Cory Hurd

ISSN 2328-0328 (online)
http://doi.org/10.3133/sir20175022C